TDGL Simulations of Critical Current Densities Across Superconducting Josephson Junction Arrays

David Caro

April 2025

A master's thesis submitted in partial fulfilment of the degree of Master of Physics (MPhys)

Supervised by Prof. Damian P. Hampshire

This master's thesis is a computational investigation into the magnetic field dependency of the critical current density $J_c(B)$ for Josephson junction arrays within applied transverse magnetic fields over a range of material properties and array geometries. We present the normalised time dependent Ginzburg-Landau (TDGL) equations used as the theoretical basis for modelling superconductors and describe the discretisation techniques and computational methods used in our code. We present results of simple Josephson junctions with varying barrier condensation parameters and demonstrate good agreement with analytical solutions in literature. We also show that, within certain limits, these systems demonstrate strong optical equivalents. From this, we present new data for junction arrays, along with qualitative and empirical methods used to model the critical current densities of these systems. We show that, in low fields for weakly coupled arrays of narrow parallel junctions with high κ values, where the order parameter is sufficiently suppressed across the normal barriers and the local magnetic field approximates the applied magnetic field. These systems provide good agreement with empirical solutions combining junction and double-slit quantitative models.





Durham University Superconductivity Group

Durham University

1 Introduction **1**

2 Thermodynamic Ginzburg-Landau Theory for Superconductivity **3**
2.1 The Ginzburg-Landau Equations 3
2.2 Type-II Superconductors & Fundamental Superconducting Scales 5
2.3 Time Dependent Ginzburg-Landau Equations & Normalisation 6

3 Computational Methodology **8**
3.1 Numerical Methods, Discretisation & Multigrid Programming 8
3.1.1 Gropp et al. Covariant Derivative & Computational Mesh 8
3.1.2 The TDGL Equations Discretisation 9
3.1.3 Multigrid Programming 10
3.2 Program Methodology 11
3.2.1 Initialising the System 11
3.2.2 Electric field Characteristics 12
3.2.3 Adaptive Coarse & Fine Ramp 13

4 Josephson Junction Critical Current Densities **14**
4.1 Analytical Solutions 14
4.1.1 Weakly Coupled Narrow Systems 15
4.1.2 Josephson Junction Diffraction and Loop Interference 16
4.2 Altering Material Properties 18
4.3 Junction Arrays 19
4.3.1 Junctions in Series and Parallel 20
4.3.2 Optical Analogues 23

5 Conclusions & Further Work **24**

References **26**

Appendix **29**

A NCC GPU Computing & Example Code **29**

B Trialled Ramping Methods **30**

C Additional Array & Junction Data **31**

List of Figures

2.i Thermodynamic free energy 4
3.i Computational cell 9
3.ii 2D computational domain 12
3.iii Thin anisotropic film current-field characteristics 13
3.iv Computational output 14
4.i Short and long junction solutions 17
4.ii Varying the barrier condensation parameter 19
4.iii Junction array visualisation and critical current density 20
4.iv Junctions in series 21
4.v Junctions in parallel 22
4.vi Weakly-coupled parallel junction 24
B.i Linear ramping 31
B.ii Exponential ramping 31
C.i $\alpha_n = -1$ $(2, 2)$ array 31
C.ii $\alpha_n = -50$ $(2, 2)$ array 32
C.iii Short junction solution 32

List of Tables

I Units of the normalised TDGL equations 8
II Values of the optimised dimensions for the $(1, 2)$ junction array 24

1 Introduction

Heike K. Onnes discovered the property of superconductivity in 1911 [1], just three years after he first produced the cryogenic techniques necessary to liquefy helium at 4.2 K. Once a superconductor is cooled below its transition temperature, T_c, it displays two unique characteristics of the material. First, that the state has zero electrical resistivity and the second, the total expulsion of magnetic flux from within the superconducting bulk, known as the Meissner state. Since then, these remarkable phenomena have enthralled scientists, both those that are dedicated to uncovering its unfamiliar physical origins and those eager for breakthroughs in commercial technologies. This included Onnes; however he quickly discovered that, in addition to the critical temperature T_c, superconductors also held a critical field B_c and a critical current J_c, above which the material transitioned to the normal state. Yet these limitations did not dissuade scientists whom saw the possibility of transferring power without energy loss; efficient and powerful electromagnets, which at the time were limited to large iron-cored, high current copper coils; and new methods of power generation and storage.

The next milestone was in 1933 through a discovery by Walther Meissner, observing that superconductors were perfectly diamagnetic [2]. Superconductors will prevent the penetration of an external magnetic field and will expel a previously penetrating field once transitioned into the superconducting state. The latter effect is notably distinct from a perfectly conducting material, that would exhibit a similar former effect due to Lenz's law preventing a change in the magnetic flux passing through its surface. Only 2 years later in 1935, brothers Fritz and Heinz London provided a significant quantitative description of this phenomena through a formulation of the interior electromagnetic fields with the supercurrent density. Rjabinin and Shubnikov were the first to discover the new type-II superconductor in 1937 [3], a Pb-Tl$_x$ alloy which displayed the two superconductivity types by varying x in the compound. The first fundamental theoretical framework for superconductors was provided by Vitaly Ginzburg and Lev Landau in 1950 [4]; who developed a phenomenological theory through Landau's field theory of second order phase transitions. That relies on a broad ansatz that the free energy of a system is both analytic in the order parameter and its gradients and obeys the energy symmetries of the Hamiltonian. The free energy density of the material near its critical temperature, T_c, depended on the order parameter and vector potential. It also allowed for an explanation for the difference between type-I and type-II superconductors.

The Josephson junction was discovered by its namesake Brian Josephson during his second year undergraduate study at Cambridge University in 1962 [5]. The junction consists of two superconducting electrodes separated by a normal barrier. Josephson provided an explanation for the superconducting current densities in the junction and was awarded a Nobel prize for this work in 1973. Though Josephson junctions have been studied and applied in science for nearly a half century, analytical solutions for the critical current in these systems have been limited and there has only been large strides in the field over the last two decades. From the time of Brian Josephson's research, the field was primarily aimed at studying the microscopic theory and current-voltage characteristic behind the systems. Seen in S.Shapiro's paper measuring

Josephson junctions under exposure of microwave radiation [6] and further theoretical theory of the Josephson phase by B. D. Josephson [7].

The ambitions of researchers and investors often seems to be aimed at high-temperature superconductors. However raising the critical temperature to realms where long range power transmission, motors and generators are feasible may still be many decades of development away. Indeed, there has been progress towards constructing 'room temperature' superconductors, such as a sulphur hydride system with a transition temperature of 288 K (15 °C) [8], but with the requirement of 270 GPa of pressure. The critical temperature of a superconductor, however, is not commonly the limiting property in most practical applications. In commercial systems, where superconductivity is achieved through the use of cryogenic facilities, the material must allow for sufficiently large critical current densities for their application. This includes nuclear magnetic resonance (NMR) devices, used in chemistry and particularly in the medical industry where it is known as magnetic resonance imaging (MRI). Here the strong, uniform and persistent magnetic fields are used to align the nuclear spins of ^{1}H nuclei. Allowing radio waves to image them, through their magnetic resonance with the proton nuclear spin, thereby mapping the distribution of water and fat in the human body.

In all these cases the superconducting material is polycrystalline, necessitating a type-II superconducting nature. The Josephson junction plays a fundamental role in the current academic understanding of these high-field polycrystalline superconductors, where the crystallites are modelled as Josephson junctions. The grains are in the superconducting state in standard operating conditions, thus represent the electrodes of a junction. The grain boundaries, exhibiting different material properties from the bulk, remain in the normal state and represent the normal barrier. In the next chapter we review GL theory, and build up to time dependent Ginzburg-Landau (TDGL) theory. The discretisation methods that allow for numerical computation of the TDGL equations, will be reviewed following this, involving discretisation methods developed by Gropp et al. and the novel application of multigrid programming to the field. Following from this we will discuss the methodology of the computation, including the computational hardware used to simulate the junction and the reasons for its use and the method used to determine the critical current. The results of the project will be shared, including a graphical representation of the methodology and the dependence of critical current against magnetic field for junctions with various material properties. The understanding and insight gained from our results will be discussed in detail, as well as possible extensions to this report. Finally the overall success and novel findings from this report will be laid out in the conclusion.

2 Thermodynamic Ginzburg-Landau Theory for Superconductivity

2.1 The Ginzburg-Landau Equations

Unlike the popular microscopic theory of BCS, Ginzburg-Landau theory does not attempt to provide an explanation for the occurrence of superconductivity in the material. Instead, having been derived from Landau's general theory of 2^{nd} order phase transitions, it describes the behaviour of a macroscopic, complex order parameter and the vector potential of such a superconducting material. The order parameter of the material is a generalisation of the spatially homogeneous superelectron density from the London theory, where the magnitude of the order parameter is a pseudo-wavefunction that relates to the density of superelectrons, as $|\psi(\boldsymbol{r})|^2 = n_s(\boldsymbol{r})$. The elegance of this is that it remains consistent with the view in BCS theory that, during the phase transition, electrons in the material condense into a single state and can thus be described by a common superelectron wavefunction. The success of this theory, being its application to conventional and non-conventional superconductors, derives from this generalised treatment of macroscopic properties. However, as the Taylor expansion of the order parameter is to second order, it restricts the theory's validity to temperatures sufficiently close to the phase transition T_c. Such that the fluctuation of the number density around the average value is small and that these spatial variation of $|\psi|^2$ and $\mathbf{A}$ are not too rapid. Thus by considering Landau's theory including the required symmetry breaking during phase transition; the conservation of symmetries as required by the Hamiltonian and considerations of additional energies. Then the Helmholtz free energy of the material can be expressed as a Taylor expansion of the order parameter and the kinetic and magnetic energies as such,

$$F = F_0 + \int \left[\alpha|\psi|^2 + \frac{1}{2}\beta|\psi|^4 + \frac{1}{2m^*}|\mathbf{\Pi}\psi|^2 + \frac{B^2}{2\mu_0} \right] d^3\boldsymbol{r} \tag{2.1.1}$$

where $\mathbf{\Pi} = -i\hbar\boldsymbol{\nabla} + q\mathbf{A}$ is the gauge invariant momentum operator, α and β are the Ginzburg-Landau phenomenological parameters, with $q = -2e$ and $m^* = 2m_e$ as the charge and effective mass of the superelectrons respectively. By considering the variation of the free energy with the magnitude of the order parameter, we may gain an understanding of how α and β vary. It is clear that for there to be a finite minimum in the free energy, $\beta > 0$ for all temperatures, thus may be approximated as temperature independent close to T_c. In addition to this, for this minimum to occur when $|\psi| \neq 0$ for $T < T_c$, requires that $\alpha < 0$ at these temperatures; with the free energy change between states at this minimum being the condensation energy of the system. Conversely, for this minimum to occur at $|\psi| = 0$ for $T > T_c \implies \alpha > 0$, therefore one can show that $\alpha \propto T - T_c$. The relation between the free energy and order parameter over a range of relative temperatures can be seen in Fig. 2.i. We can intuitively see here that below T_c the free energy has a local minimum for non zero $|\psi|$, ensuring that the superconducting phase is energetically favourable, while above T_c no such minimum exists for $|\psi| > 0$, so the normal state is favourable, as required.

Through the minimisation of the free energy with respect to $|\psi|^2$, we find a normalisation value of the order parameter as,

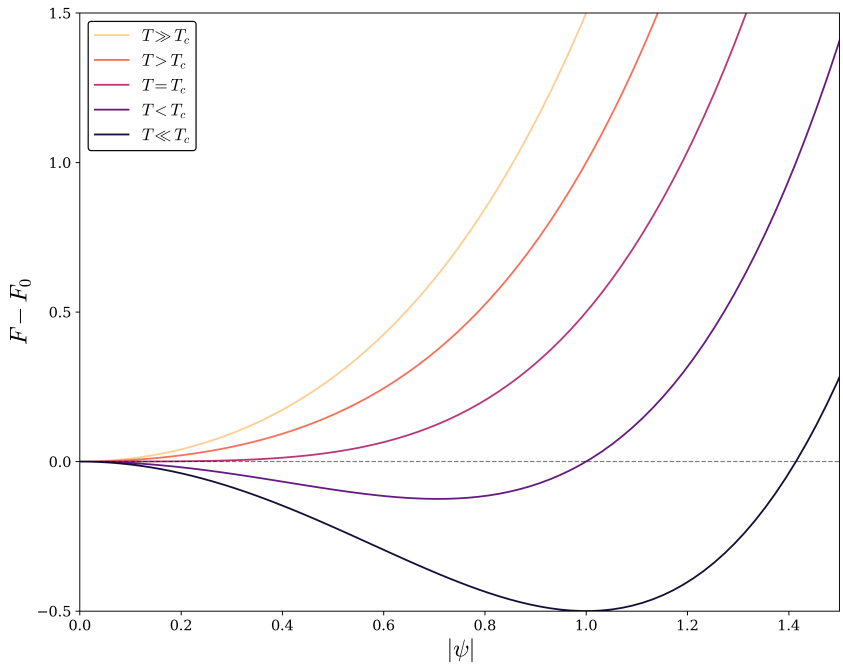


FIG. 2.i: The free energy of a superconductor, in no magnetic field and at equilibrium, as a function of the second order Taylor expansion of $|\psi|$, with relative temperatures ranging from far larger to far smaller than T_c

$$\frac{\partial F_s}{\partial |\psi|^2} = 0 \implies |\psi_0|^2 = -\frac{\alpha}{\beta} \tag{2.1.2}$$

It should be noted that this is the value of the order parameter only when $|\psi(\boldsymbol{r})|^2$ approaches infinitely deep regions of the superconductor. In addition to this, these phenomenological parameters α, β, m^* are only collectively specified up to a constant of proportionality.

By applying variational minimisation of the free energy equation with respect to ψ^* and $\mathbf{A}$, the ground state of the macroscopic system and vector potential, up to a gauge transformation, may be found. The Ginzburg-Landau equations that emerge from this are a set of differential equations coupling ψ and $\mathbf{A}$. Taking the first minimisation of Eq. (2.1.1) with respect to the order parameter complex conjugate, ψ^*, given as $\frac{\partial F}{\partial \psi^*} = 0$, provides the first GL equation [4],

$$-\frac{\hbar^2}{2m}\mathbf{\Pi^2}\psi + \alpha\psi + \beta|\psi|^2\psi = 0 \tag{2.1.3}$$

with the corresponding, insulating, boundary condition being,

$$\mathbf{n} \cdot \mathbf{\Pi}\psi = 0 \tag{2.1.4}$$

at the surface of the superconductor with an outward normal unit vector $\mathbf{n}$ and is only valid for an interface between a superconductor and an insulator, enforcing that no current passes through the surface. The equation, Eq. (2.1.5), can be seen to be similar to the time-independent Schroedinger equation for a particle with mass $m = 2m_e^*$ and charge $q = -2e$, but with the nonlinear $\beta|\psi|^2$ term. With no nonlinear term, the particle would have an energy eigenvalue of

$-\alpha$. Instead, this term acts as a repulsive potential of ψ on itself, leading to the wavefunction, $\psi(\boldsymbol{r})$, to spread out uniformly in space [9]. In a similar manner, one can consider the fluctuations of the magnetic vector potential in relation to Maxwell's fourth equation, by $\frac{\partial F}{\partial \mathbf{A}} = \mu_0 \mathbf{J}_{\text{app}}$, to gain the second equation [4],

$$\mathbf{J}_{\text{s}} = -\frac{iq\hbar}{2m}\left(\psi^* \boldsymbol{\nabla}\psi - \psi \boldsymbol{\nabla}\psi^*\right) - \frac{q^2}{m}|\psi|^2\mathbf{A} = \frac{q\hbar}{m}\text{Im}\left\{\psi^*(\boldsymbol{\Pi} - \frac{iq}{\hbar}\mathbf{A})\psi\right\} \tag{2.1.5}$$

2.2 Type-II Superconductors & Fundamental Superconducting Scales

It is important now to introduce the characteristic length scales over which the order parameter magnitude and magnetic field vary. With these we may define the characteristics of Type-II superconductors and distinguish it from Type-I, as well provide us with variables to normalise our equations with. First, let us consider a superconducting flat slab, infinite in extent in the y, z and $x > 0$ directions, and in contact with a conductive metal occupying the region $x < 0$ in a similar manner. The first GL equation Eq. (2.1.3) for this system will reduce to a 1D equation; which, in absence of electric and magnetic fields such that $\mathbf{A} = 0$, leads to,

$$-\frac{\hbar^2}{2m}\frac{\partial^2\psi}{\partial x^2} + (\alpha + \beta|\psi|^2)\psi = 0 \tag{2.2.1}$$

At the interface the order parameter will be suppressed, $\psi(0) \approx 0$, while deep within the superconductor it will reach its Meissner value $\psi \to \psi_0$ given by Eq. (2.1.2) and be constant in space $\partial_x\psi \to 0$. The order parameter can be solved to give,

$$\psi(x) = \psi_0 \tanh\left(\frac{x}{\sqrt{2}\xi}\right) \tag{2.2.2}$$

Where we have defined the coherence length to be,

$$\xi^2 = \frac{\hbar^2}{2m|\alpha|} \tag{2.2.3}$$

Thus this variable describes the length scale over which the order parameter varies. It is notably temperature dependent, through $\alpha \propto T - T_c$, and diverges at the critical temperature. Next, we can consider the second GL equation, Eq. (2.1.5), within the bulk of the superconductor. Where, as mentioned, the gradient terms do not contribute and the order parameter takes the bulk equilibrium value. This leads to the result,

$$\mathbf{J}_{\text{s}} = -\frac{q^2}{m}|\psi_0|^2\mathbf{A} \tag{2.2.4}$$

Taking the curl of the equation and using Maxwell's second and fourth equations as well as vector identities and assuming that the superelectrons take the charge of Cooper pairs of $q = -2e$ leads to the result,

$$\boldsymbol{\nabla}^2\mathbf{B} = \frac{4\mu_0 e^2}{m}|\psi_0|^2\mathbf{B} \tag{2.2.5}$$

The penetration depth is thus defined to be,

$$\lambda^2 = \frac{m}{4\mu_0 e^2 |\psi_0|^2} \tag{2.2.6}$$

For our slab system, when there is a magnetic field in the z direction, the strength of the magnetic field will exponentially attenuate over the length scale λ into the superconductor along the x direction. This effect occurs due to screening currents along the boundary of superconductor and is known as the Meissner state; where applied fields are completely excluded from the bulk of the superconductor, with a homogenous order parameter inside the bulk. Finally we can introduce the Ginzburg Landau parameter, that describes the ratio of these two lengths,

$$\kappa = \frac{\lambda}{\xi} \tag{2.2.7}$$

This parameter provides the distinguishing feature between Type I and Type II behaviour. At the interface between the superconducting and normal phases of a material in an external field. The surface free energy, $\sigma_{\mathrm{NS}} \approx \frac{B_c^2}{2\mu_0}(\xi_s - \lambda_s)$, at this boundary is positive for kappa values of $\kappa \leq 1/\sqrt{2}$ and negative when $\kappa > 1/\sqrt{2}$; as shown by Ginzburg and Landau in their seminal paper in 1950 [4]. Thus, for superconductors with negative surface free energy, it will be energetically favourable to form these interfaces. This typifies Type-II superconductors which experience a mixed state above the lower critical field $B_{c1} < B_c$, allowing the penetration of flux as fluxons and an increasing the NS interfacial surface area. Naturally Type-I superconductors, with $\kappa \leq 1/\sqrt{2}$, do not experience this effect and transition directly from the superconducting Meissner state to the normal state.

2.3 Time Dependent Ginzburg-Landau Equations & Normalisation

The form of the time dependent equations are not unique in literature, but the most well accepted equations, which we use in computation, were first derived by Schmid [10]. Gor'kov and Eliashberg then rigorously proved this as a limiting case of BCS theory in the gapless regime [11]. The range of validity of these equations is far narrower in scope than the static counterpart. Firstly, like its counterpart, it is derived from perturbative techniques, so we must remain close to the critical temperature. But in addition we also require that the deviations from equilibrium are suitably small. This is typically only achieved in gapless superconductors, where there is no band gap between superelectron and normal electron states, $\Delta = 0$. Here the relaxation process of the order parameter, characterised by the added phenomenological parameter Γ, is slow compared to the electronic energy scales of the system. The equations were then written in normalised form to produce the well accepted version by Hu and Thompson [12], which we will arrive at later. There have been other approaches to provide a more generalised theory, which include the energy gap of superconductors, but these have yet to be accepted by the community.

The motivation of the equations made by Schmid, of phenomenological parameter Γ, was to characterise how quickly the order parameter relaxes into the equilibrium state from small perturbations. A gauge invariant time dependence, with the proportionality factor Γ, describes the relaxation towards the first GL equation, Eq. (2.1.3), and written as,

$$-\Gamma\left(\frac{\partial}{\partial t}-\frac{iq}{\hbar}\varphi\right)\psi=\frac{\delta F_s}{\delta\psi^*}. \tag{2.3.1}$$

Where φ is the scalar potential used to maintain gauge invariance. The second GL equation is generalised to include currents produced by normal electrons in the presence of an electric field such that the total current in the material is described as,

$$\mathbf{J}=\mathbf{J}_{\rm app}+\mathbf{J}_{\rm n}+\mathbf{J}_{\rm s} \tag{2.3.2}$$

where $\mathbf{J}_{\rm app}$ is the applied current given by Maxwell's fourth law, $\mathbf{J}_{\rm n}$ is the normal current given by Ohm's law and $\mathbf{J}_{\rm s}$ is given by the second GL equation, Eq. (2.1.5). In order to normalise the equations, all the material parameters are normalised to that of the bulk superconductor, with the bulk Meissner value ψ_0 used to normalise the order parameter. The time and length scales in the system are normalised to the superelectron relaxation time τ and the superconducting coherence length $\xi_{\rm s}$ respectively. Inserting these values into the first GL equation Eq. (2.1.3), provides a normalisation value for the vector potential, A_0. With these one can derive the normalisation value for the current J_0, by inserting them into the second GL equation, Eq. (2.1.5). Finally magnetic fields are normalised to the upper critical field $B_{\rm c2}$. These normalisations, and others that are possible by using those mentioned in derivation, are summarised in Table. I. Finally the resulting first TDGL equation in normalised form is written as,

$$\eta\left(\frac{\partial}{\partial t}+i\varphi\right)\psi=\left[\frac{1}{m(\boldsymbol{r})}(\boldsymbol{\nabla}-i\mathbf{A})^2+\alpha(\boldsymbol{r})-\beta(\boldsymbol{r})|\psi|^2\right]\psi \tag{2.3.3}$$

where $\psi=\psi(\boldsymbol{r})$ is the scalar field representing the order parameter within the material. The material parameters $\alpha,\ \beta$ and $m^{-1}=\langle m_i^{-1}\rangle,\ i\in\{x,y,z\}$ are normalised to the superconducting parameters $\alpha_s,\ \beta_s,\ (m_s^{-1})_x$. The second equation is given as,

$$\sigma\left(\frac{\partial\mathbf{A}}{\partial t}+\boldsymbol{\nabla}\varphi\right)=-\kappa^2\boldsymbol{\nabla}\times\boldsymbol{\nabla}\times\mathbf{A}+m^{-1}(\boldsymbol{r})\,\mathrm{Im}\left[\psi^*(\boldsymbol{\nabla}-i\mathbf{A})\psi\right] \tag{2.3.4}$$

The first term can be seen to be normalised versions of Ohm's law and the second as Maxwell's fourth equation in the absence of a time-varying electric field. The associated boundary conditions for both equations are given as;

$$(\boldsymbol{\nabla}\times\mathbf{A}-\mathbf{B}_{\rm app})\times\hat{\mathbf{n}}=0, \tag{2.3.5}$$

$$(\boldsymbol{\nabla}-i\mathbf{A})\psi\cdot\hat{\mathbf{n}}=-\frac{1}{b}\psi. \tag{2.3.6}$$

Where b is the De Gennes extrapolation length [13] in normalised units. The first condition ensures that there is no tangential component of the applied and internal magnetic vector with the surface of the material (i.e magnetic field continuity). While the second is a generalisation of the boundary condition for the first GL equation which describes the flow of current with a non-superconducting surfaces, i.e for highly insulating surfaces $b\to\infty$.

Symbol	Units	Description
$\boldsymbol{r}$	$\xi_s = \hbar/\sqrt{2m_s\lvert\alpha_s\rvert}$	Coherence length
t	$\tau = \mu_0\sigma_n\lambda_s^2$	Electronic relaxation time
ψ	$\lvert\psi_0\rvert = \sqrt{\lvert\alpha_s\rvert/\beta_s}$	Order parameter
$\mathbf{A}$	$A_0 = \phi_0 2\pi\xi_s$	Vector potential
φ	$\varphi_0 = \phi_0/2\pi\tau$	Scalar potential
$\mathbf{B}$	$B_{c2} = \phi_0/2\pi\xi_s^2$	Upper critical field
$\mathbf{E}$	$E_0 = \phi_0/2\pi\tau\xi_s$	Electric field scale
$\mathbf{J}$	$J_0 = \phi_0/2\pi\mu_0\kappa\xi_s^3$	Supercurrent density scale

TABLE I: Units of the normalised TDGL equations

3 Computational Methodology

3.1 Numerical Methods, Discretisation & Multigrid Programming

3.1.1 Gropp et al. Covariant Derivative & Computational Mesh

The discretisation method used in the code is based on the work from Gropp et al. [14], with modifications developed by Winiecki et al. [15] and then Blair. The underlying method for spatial discretisation is through the use of link variables to discretise the gauge invariant covariant derivatives, $\boldsymbol{\nabla} - i\mathbf{A}$ in the TDGL equations. These methods have been extensively well reviewed in previous papers by Blair [16] and Din [17], but we will review the methods first formulated by Gropp et al. to understand how these equations are discretised onto a computational mesh and linearised and applied in multigrid methods in the MulTDGL package written by Haddon [18].

In order to numerically solve the TDGL equations Gropp et al. first set the electric potential gauge to be zero, $\varphi = 0$, in order to simplify the equations. After which they introduced a 3D auxiliary vector formed of the link variables, $\boldsymbol{U} = (U_x, U_y, U_z)$, with each link defined as,

$$U_\mu(\boldsymbol{r}) = \exp\left(-i\int_{\mu_0}^{\mu} A^\mu(x,y,z)\, d\mu'\right)\hat{\boldsymbol{e}}_\mu \tag{3.1.1}$$

with $\mu \in \{x, y, z\}$ being a coordinate axes and $\boldsymbol{r} = (x, y, z)$ the position. These formed a complex, unimodular set, with the phase defined as the integration of the vector potential along a particular axis between two reference points, allowing the vector potential to be defined by its derivative. The gauge invariant discretisation of the covariant derivatives to first order can then be expressed as;

$$(\boldsymbol{\nabla} - i\mathbf{A})\,\psi(\boldsymbol{r}) = \sum_\mu U_\mu^* \frac{\partial}{\partial\mu}(U_\mu\psi)\,\hat{\boldsymbol{e}}_\mu \tag{3.1.2}$$

and to second order, representing the gauge invariant kinetic term, as,

$$(\boldsymbol{\nabla} - i\mathbf{A})^2\,\psi(\boldsymbol{r}) = \sum_{\mu} U_{\mu}^{*}\frac{\partial^2}{\partial\mu^2}(U_{\mu}\psi)\,\hat{\boldsymbol{e}}_{\mu} \tag{3.1.3}$$

To employ these definitions in a finite difference method, requires the discretisation of the simulation space into a structured mesh such that the position vector $\boldsymbol{r}_{i,j,k}$ takes explicit values within the range: $i \in [1, n_x],\ j \in [1, n_y],\ k \in [1, n_z]$, with locations separated by step sizes h_{μ}. This results in a grid with nodes defining the order parameter and links defining the magnetic field. The normalised material properties $\alpha,\ \beta$ are also defined on these nodes, such node variables are:

$$\psi_{i,j,k} = \psi(\boldsymbol{r}_{i,j,k}), \quad \alpha_{i,j,k} = \alpha(\boldsymbol{r}_{i,j,k}), \quad \beta_{i,j,k} = \beta(\boldsymbol{r}_{i,j,k}) \tag{3.1.4}$$

The discretised effective mass is taken as an average over two adjacent points and defined on the links in the mesh. A diagram of a 'cell' in the computational domain can be seen in Fig. 3.i, where the link variable of the unimodular phase $e^{-ia_{\mu}}$ and effective mass given as:

$$a^{\mu}_{i,j,k} = a_{\mu}(\boldsymbol{r}_{i,j,k}) - a_{\mu}(\boldsymbol{r}_{i,j,k} + h_{\mu}\hat{\boldsymbol{e}}_{\mu}) \tag{3.1.5}$$

$$(m^{-1}_{i,j,k})^{\mu} = \frac{1}{h_{\mu}}\int_{r_{i,j,k}}^{r_{i,j,k}+h_{\mu}\hat{\boldsymbol{e}}_{\mu}} m_{\mu\mu}\,d\mu' \tag{3.1.6}$$

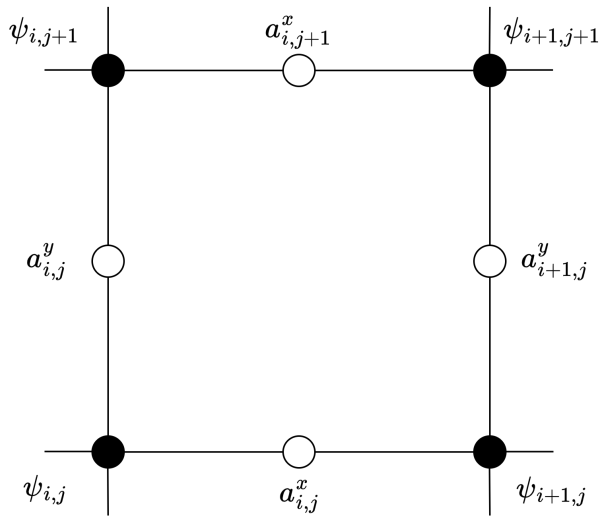


FIG. 3.i: A diagram of the computational unit cell, where the order parameter value is discretised onto nodes (black circles), with indices i, j in the x, y directions respectively and the link variables are defined on links (open circles) between nodes.

3.1.2 The TDGL Equations Discretisation

The descritsation of the TDGL equations we follow are through the work of C. Haddon [18], where unlike Gropp et al. the London gauge, $\nabla \cdot A = 0$ is maintined in the TDGL equations.

This means that, following discretisation, the TDGL equations are of the form of elliptic PDEs, specifically heat equations, and thus more amenable to multigrid iterative methods. Similarly to Gropp and Winiecki, Haddon employs a second order central difference method using link variables for spatial discretisation, but instead for the purposes of multigrid computation, uses backwards Euler for temporal discretisation. Using $I = (i, j)$ to denote a grid point and δ_ν to denote an index step, where $(I + \delta_x)_x = i + 1$, with the value of $|\psi|^2$ at the last time step to linearise the equation. The first discretised TDGL equation, Eq. (2.3.3), can be written is:

$$\frac{\psi_I^1 - \psi_I^0 \exp\left[-i\delta t\, \varphi_I^0\right]}{\delta t} = \left(\alpha_I - \beta_I |\psi_I^0|^2\right) \psi_I^1 \tag{3.1.7}$$

$$+ \frac{1}{h^2} \sum_\nu \Big\{ (m_I^{-1})^\nu \left[U_I^\nu\, \psi_{I+\delta_\nu}^1 - \psi_I^1\right] \tag{3.1.8}$$

$$+ (m_{I-\delta_\nu}^{-1})^\nu \left[(U_{I-\delta_\nu}^*)^\nu\, \psi_{I-\delta_\nu}^1 - \psi_I^1\right] \Big\} \tag{3.1.9}$$

where $0, 1$ denote the variables from the previous and current step respectively and δt as the time step. The second equation Eq. (2.3.4) can be written as,

$$-\sigma \left(\frac{A_I^1 - A_I^0}{\delta t} + \frac{1}{h^2} \sum_\nu \left[(m_I^{-1})^\nu \left(\varphi_{I+\delta_\nu}^1 - \varphi_I^1\right) + (m_{I-\delta_\nu}^{-1})^\nu \left(\varphi_{I-\delta_\nu}^1 - \varphi_I^1\right) \right] \right) \tag{3.1.10}$$

$$= -\frac{\kappa^2}{h^2} \sum_\nu A_{I+\delta_\nu}^1 + A_{I-\delta_\nu}^1 - 2A_I^1 + \frac{1}{h^2} \mathrm{Im} \left\{ (\psi_I^*)^1 \sum_\nu (m_I^{-1})^\nu\, U_I^\nu\, \psi_{I+\delta_\nu}^1 + (m_{I-\delta_\nu}^{-1})^\nu\, (U_I^*)^\nu\, \psi_{I-\delta_\nu}^1 \right\} \tag{3.1.11}$$

Where we have used the central difference method to discretise the scalar and vector potentials. As the finite difference calculation requires edges, $U_I^\nu, (m_I^{-1})^\nu$, and nodes, ψ_I^ν, to be defined around each point. Similarly to Winiecki [15] and Blair [16], Haddon enforced periodic boundary conditions in the x-direction and ghost points in y-direction as described by [19] and [20]. Ghost points are not in the measured computational domain but an extra set of are artificial links and nodes added to the final row of nodes for numerical calculations and to enforce the insulating boundary condition in the y-direction (where $b \to \infty$ in Eq. (2.3.5)). Periodic boundary conditions in the x direction requires that the last set of nodes and x and y links in the x-direction are equal to the first set of nodes and links. This can be expressed as $p_{n_x,j} = p_{0,j}$ and $p_{n_x+1,j} = p_{1,j}$, where $p \in \{\psi, U^x, U^y\}$.

3.1.3 Multigrid Programming

The MulTDGL package developed by Charles. P. Haddon [18], stands out through its novel use of multigrid methods to iteratively evolve the TDGL equations faster and more efficiently than previous methods; such as the Crank-Nicolson method used in Winiecki [15] or explicit forward Euler method in Gropp [14]. In particular, it allows for far greater scalability, with time scaling on the order of $O(n)$ links and experiences less build up in numerical noise due to the equations being solved across a variety of grid resolutions at each time step.

For a arbitrary linear equation of the form $L\psi = f(\varphi)$, where both L, a linear discrete-Laplacian operator, and the solution $f(\psi)$ are known. Then given an initial guess $\psi_e = \psi + \varepsilon$, with the error ε and solution $f(\varphi_e)$; the difference between the correct and approximate solutions, known as the residual, $r = f(\varphi) - f(\varphi_e)$, can be given by the important residual equation $L\varepsilon = r$. Using this relation, Gauss-Seidel iteration of this linear equation can be performed on each grid, with the residual solutions transferred between each. This iteration requires equations to be linearised into a matrix form, with the matrix elements solved for a single step from k to $k+1$ for each iteration.

In order to effectively coarsen grids, the sides of the grids must be size 2^n, where n grids can be formed with half the resolution of the previous grid by removing every other row and column. As mentioned we must solve the residual equation on each grid and then transfer the solution between grids. To do this we use linear interpolation to transfer the coarse solution to the fine grid, with the coarsening operator being the transpose this operator. A single time step consists of solving Eq. (3.1.7) for ψ_I^1, taking a backward Euler time step for the current density and then solving Eq. (3.1.10); both solutions are found using red-black Gauss-Seidel smoothing. One multigrid step then consists of calculating ψ on the fine grid with an initial guess ψ_e, calculating the residual and transferring or 'restricting' this to a coarser grid. Then iterating the equation again using a initial guess ε and transferring or 'interpolating' this residual back to the finer grid and correcting ψ_e with it. Finally the full n-grid V cycle repeats this process for φ and then A until the discretised equations have been solved to within tolerance.

3.2 Program Methodology

3.2.1 Initialising the System

In Fig. 3.ii we display a square superconducting electrode of length l_s and width w_s, with normalised material parameters of $\alpha_s = \beta_s = m_s = 1$. The junction has a thickness of d_n and there is a coating width of w_c, both of these regions have the same material properties of α_n, β_n and m_n. The total size of the system is then $l = l_s + d_n$ in the x direction and $w = w_s + w_c$ in the y direction. The system is set by initialising the entire system to take the superconducting material parameters, and then the location of the normal regions are specified by setting the indices of the 2D Julia array where $\alpha = \alpha_n$ and $m = m_n$. In addition to this normal-superconducting (NS) interfaces of the two regions are set to be single columns or rows in the direction of the interface, where the material properties of the two regions have been averaged.

Arrays are then be generated using this geometry as a unit cell. In order to replicate the structure of polycrystalline superconductors, where the superconducting electrodes represent grains; the coatings are set to be the same width as the barrier thickness, representing grain boundaries. This unit cell is then repeated in the x and y directions as necessary. To maintain uniform distance between electrodes in the x and y directions, each barrier on the upper and lower sides of the junction unit cell are half of the chemical thickness of the junction, d_n. Any additional coating is then added to the edges of the array, with the total width of the coating on

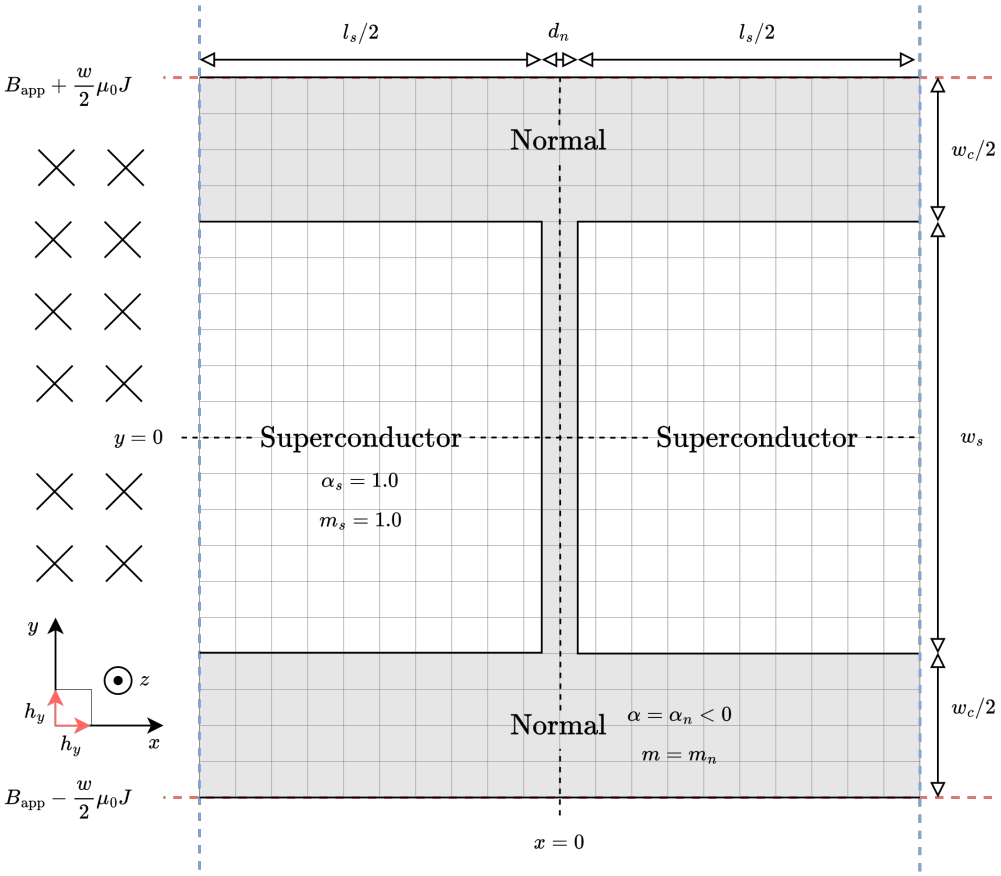


FIG. 3.ii: Schematic of the 2D computational domain. The axes (shown in bottom left) of the system are centred at the origin of the computational domain. The direction of the applied magnetic field is indicated by crosses on the left hand side, with the magnetic field at the edges of the domain in the y direction, to produce a field differential, labelled. The electrode width is indicated by w_s, with length l_s, the thickness of the normal barrier is indicated by d_n, with coating width w_c. Periodic boundary conditions in the x direction are indicated by blue dashed lines, with insulating boundary conditions in the y direction indicated by red dashed liens

one side being the sum of the padding and half the barrier thickness $w_c = w_{\text{ext}} + d_n/2$. This method however has the drawback of requiring all array systems to have an outer coating of at least half the barrier thickness.

3.2.2 Electric field Characteristics

The most simple implementation of the code is to use it to understand the regimes of a superconductor as it transitions into the normal phase through a continual linear current ramp and produce voltage-current plots common in experimentation.. The time step is set to $\delta t = 0.5\tau$ and is first initialised in the Meissner state so that $|\psi| = 1$ everywhere and the phase randomised across the system to provide initial values for Gauss-Seidel relaxation. After which point, the magnetic field is ramped at a small and constant rate of $5 \times 10^{-2} B_{c2}\tau^{-1}$ until the desired field is reached. To allow the system to return to equilibrium before the current is ramped, the system is settled for a period of $t_{\text{settle}} = 2.5 \times 10^2 \tau$. Finally the current is ramped at a rate of

$3 \times 10^{-4} J_{\mathrm{D}} \tau^{-1}$, up to $1.2 J_{\mathrm{D}}$, well beyond the maximum current density. The average electric field in the x direction, $\langle E_x \rangle$, in the system is calculated between two time steps. This was repeated through a range of fields up to $1.5 B_{\mathrm{c2}}$ in steps of $0.3 B_{\mathrm{c2}}$. The critical current density is then determined to be the point where $\langle E_x \rangle$ in the system is no longer null valued but begins to oscillate in time. From Fig. 3.iii we can see that under no magnetic field, this can be seen to occur at $\sim 0.9 J_D$

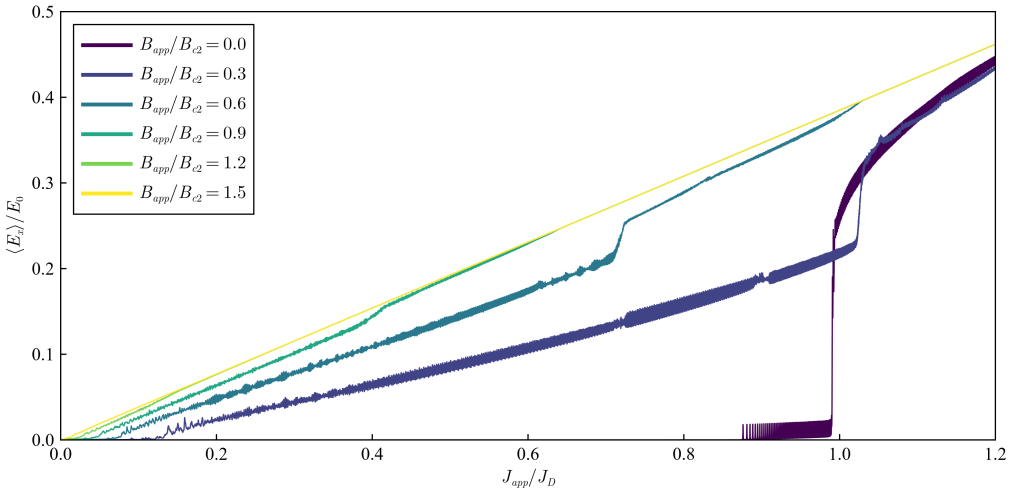


FIG. 3.iii: Current-field characteristics for a thin anisotropic superconducting film, with no coating, of width $20\xi_s$, length $60\xi_s$ and a weak superconducting barrier of thickness $2\xi_s$. With superconducting material parameters of $\kappa = 10$, $m_e = 1$, with $\alpha_s = 0.8$ for the central barrier and $\alpha_s = 1.0$ for the rest of the material. Periodic boundaries exist in the x direction and insulating boundary conditions in the y direction.

For systems within a large applied field the material hits the resistive state at a far lower current and for a field of $1.5 B_{c2}$ it immediately transitions to the normal ohmic state. However you can spot that for a field of $1.2 B_{c2}$, this transition is not immediate, even though we are well above the upper critical field. This is due to the presence of the effective upper critical field B^*_{c2} (which we will not discuss in depth), that allows for superconductivity to persist within a thin sheath region of a few coherence lengths near insulating surfaces. The exact field varies between systems depending on the different interfaces in the material and whether they are normal or insulating, as seen by the work of Din [17].

3.2.3 Adaptive Coarse & Fine Ramp

A number of ramping method were trialled in order to determine the critical current of the system in the most efficient way. What was settled upon was a combination of linear and exponential ramping methods and making use of a suggestion at the end of Din's thesis. Here the system is initialised in the same way as the continuous ramp, after which point the current would first be ramped at a large exponential rate from a low initial value $j_{\mathbf{init}} = 10^{-6} J_D$ and

with a step ratio of $r = 1.15$, allowing the full current range (from $10^{-6} \rightarrow 1J_D$) to be traversed in under 100 steps. If the spatially average electric field exceeded a criterion value of $10^{-5}E_0$, the system would be held at that current value to allow transient effects to equilibrate. When a persistent electric field was maintained in the system for a time longer than $t_{hold1} = 1 \times 10^3\tau$, the ramping is 'tripped' and the system is returned to the state and current at the step before tripping, providing a lower bound of the critical current. After this point the current is ramped from this lower bound in linear steps of $j_{\text{ramp}} = 1 \times 10^{-4}J_D\tau$ until the critical current is found, indicated by $\langle E_x \rangle > E_c = 10^{-5}E_0$ for a period longer than $t_{\text{hold2}} = 2.5 \times 10^{-3}\tau$. A typical computation output for this method is shown in Fig. 3.iv.

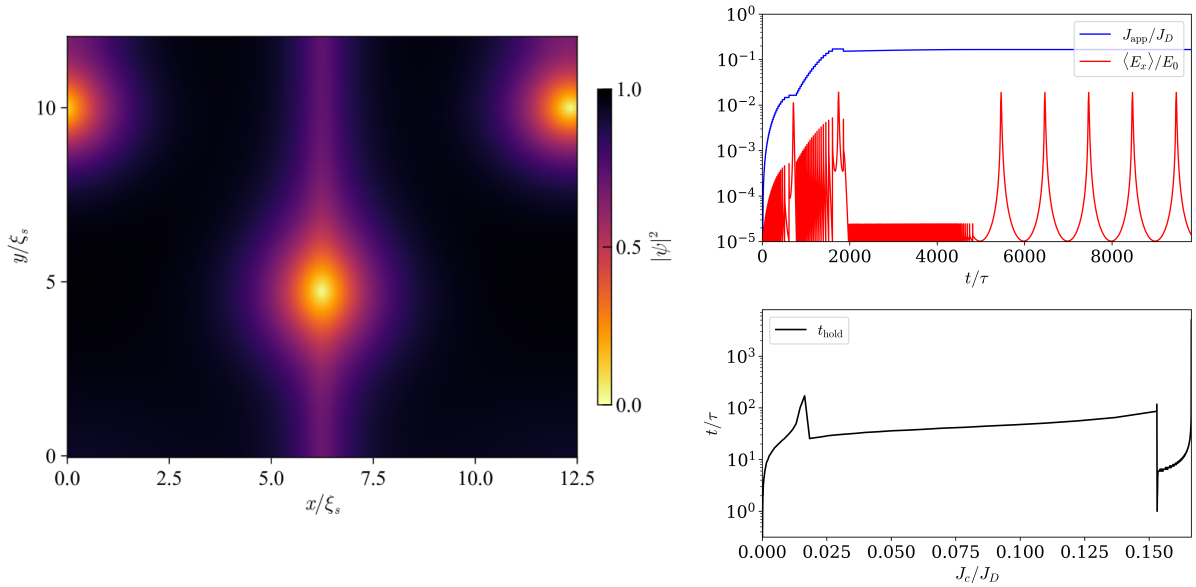


FIG. 3.iv: Left: the normalised superelectron density in a $12\xi_s$ by $12.5\xi_s$ system at $0.1B_{c2}$ and $0.15J_D$. Right top: A plot of the electric current and current density in a typical simulation to determine the critical current of the system. Right bottom: plot of the hold time required after each ramping step with logarithmic scale on the y axis.

4 Josephson Junction Critical Current Densities

4.1 Analytical Solutions

Analytical solutions for the critical current densities of Josephson Junctions were not the subject of widespread academic research for many years. However solutions for fundamental junction geometries have been built up through work by important figures in the field such as Clem, Saint-James, de Gennes and Tinkham; as well as those at the Durham Superconductivity group, namely Hampshire, Blair and Din. Much of their work and analytical solutions will provide the basis for confirming that the computational data in this paper is correct.

The solutions relevant to the geometries studied in this thesis are based on narrow, weakly coupled junctions, where $|\alpha_n d_n| \gg 1$, so that the order parameter is heavily suppressed across

the junction and allowing for easier penetration of flux. With geometries where the statement $\xi_s \ll w_s \ll \lambda_s$ is valid, such that under our normalisation scheme, where $\lambda_s = \kappa_s$, this statement assumes that the magnetic field is uniform across the junction. Much of this will be from the works of Clem [21] and Blair [22]. In addition to this, from our restriction that the barrier thickness represents polycrystalline grain boundaries, this will remove a degree of freedom in our geometries and we will leave the thickness constant, commonly $d_n = 0.5\xi_s$, and only alter the normal material condensation parameter α_n in our work. While our investigation only into narrow junctions reflect the fact that common superconducting materials have high κ values. This value of course reduces with increased operating temperatures, but for many applications it still remain very high, as shown by research by B. Bonin [23] for superconducting RF cavities. As such we hope to work in a regime that has as much relevance to industrial superconductors as we are able to. However it is important to note that we will only be looking at the critical current of junctions in low fields, unlike much of the work by Din [17], which is a distinct departure from the motivation of our work, but has been required due to time enforced limits for our data collection.

4.1.1 Weakly Coupled Narrow Systems

First in order to provide a basis for our analytical solutions we shall define the gauge invariant phase γ, with its a spatial gradient of,

$$\boldsymbol{\nabla}\gamma = \boldsymbol{\nabla}\theta - \mathbf{A} \tag{4.1.1}$$

Through a consideration of the gauge invariant equations using this phase and the order parameter with the usual form of $\psi = |\psi|e^{i\theta}$, lead Josephson to propose a relation for the voltage-current characteristics he saw across junctions he studied in low fields and currents. He proposed his relation as,

$$J_c = J_{DJ}\sin(\Delta\gamma) \tag{4.1.2}$$

Where J_{DJ} is the maximum theoretical current for the Josephson junction and $\Delta\gamma$ is the difference in the gauge invariant phase across the junction, which will maximise the current to be the depairing current at $(n+1)\pi/2$. For narrow weakly coupled junctions in low fields in a perpendicular magnetic field, this phase difference varies across the width of the junction (in the y direction of our diagram Fig. 3.ii) in a sinusoidal fashion, as given by the direction of the vector potential in the junction. This phase relation was found by Clem [21] and given as,

$$\Delta\gamma(y) = \Delta\gamma(0) + \frac{2\pi B_{\mathrm{app}} y d_{\mathrm{eff}}}{\phi_0} + \frac{16\pi B_{\mathrm{app}}}{\phi_0 w_s}\left(\sum_{n=0}^{\infty}\frac{(-1)^n}{k_n^3}\tanh\left(\frac{k_n l_s}{2}\right)\sin(\mathrm{k_n y})\right) \tag{4.1.3}$$

Where $k_n = (2n+1)/w_s$, here d_{eff} represents the effective area of the junction that the magnetic field penetrates due to the screening current in a narrow junction. This accounts for the reduction in the order parameter on either side of the junction on the scale of a coherence length. It is important to also make note again that all variables, including junction dimensions, in this

equation are normalised, with the flux quantum being $\phi_0 = 2\pi$. The critical current density for the junction is then given as the integral of Eq. (4.1.2) across the width of the junction as,

$$J_c = \max_{\Delta\gamma(0)} \left\{ \frac{1}{w_s} \left| \int_{-w_s/2}^{w_s/2} dy J_{DJ}(0) \sin\left(\Delta\gamma(y)\right) \right| \right\} \tag{4.1.4}$$

Where $J_{DJ}(0)$ is the critical current density value in zero magnetic field and takes the value of J_c when the equations is maximised with respect to $\Delta\gamma(0)$, given as $\pm\pi/2$. This ensures that the maximum current can flow through the junction as given by Josephson's relation. The amplitude of the critical current in this framework can be reliably described by an empirical equation found by Blair, which takes the form,

$$J_{DJ}(B) \approx c_0 \left(\frac{\phi_0}{B_{app} w_s^2} \right)^{c_1} J_{DJ}(0) \tag{4.1.5}$$

where c_0 and c_1 are optimised parameters with approximate values $c_0 \approx c_1 \approx 0.58$ for an aspect ratio of 1, but does vary with the aspect ratio. The equation aims to describe the decreased spacing between vortices inside the barrier as the applied field is increased and thus the fraction of the barrier width contributing to the net critical current. This reduces the peak current density a junction can support, before destructive interference, as given by Clem's solution, is accounted for.

4.1.2 Josephson Junction Diffraction and Loop Interference

The fact that Eq. (4.1.4) has a periodic form is no coincidence. The critical current density of a junction within a magnetic field depends on the phase difference of the order parameter across the junction, which depends on the flux through the junction. We can demonstrate this well in the short and long limits of a narrow junction. For electrodes which are short relative to the junction width $l_s \ll w_s$, screening currents moving in the y direction will flow mostly parallel to the barrier. As such the Josephson vortices in the barrier are spaced approximately equally along the junction width, which will lead to a gauge invariant phase difference linear in y. This produces a critical current density with a Fraunhofer-like functional form, as seen in Blair [22],

$$J_c = J_{DJ}(0) \left| \mathrm{sinc}\left(\frac{\pi\phi'}{\phi_0} \right) \right|, \qquad \text{where } \phi' = w_s l_s B_{app} \tag{4.1.6}$$

This can be understood due to the transport current varying sinusoidally with junction width $\mathbf{J}(y)$, caused by the current vortices circulating fluxons. As such the maximum current that can flow across the junction in this field is given by the fraction of this circulating current that does not cancel with itself.

As mentioned the equation has a Fraunhofer form, specifically that of a single slit interference pattern. The phase, as seen in Eq. (4.1.6), is given as the flux through the junction, which for narrow junctions, where the penetration depth is larger than the junction dimensions, is approximately the area multiplied by the applied field. On the other hand, if the electrodes are long relative to the junction width, where $l_s \gg w_s$, and the effective junction thickness $d_{\text{eff}} \to 0$.

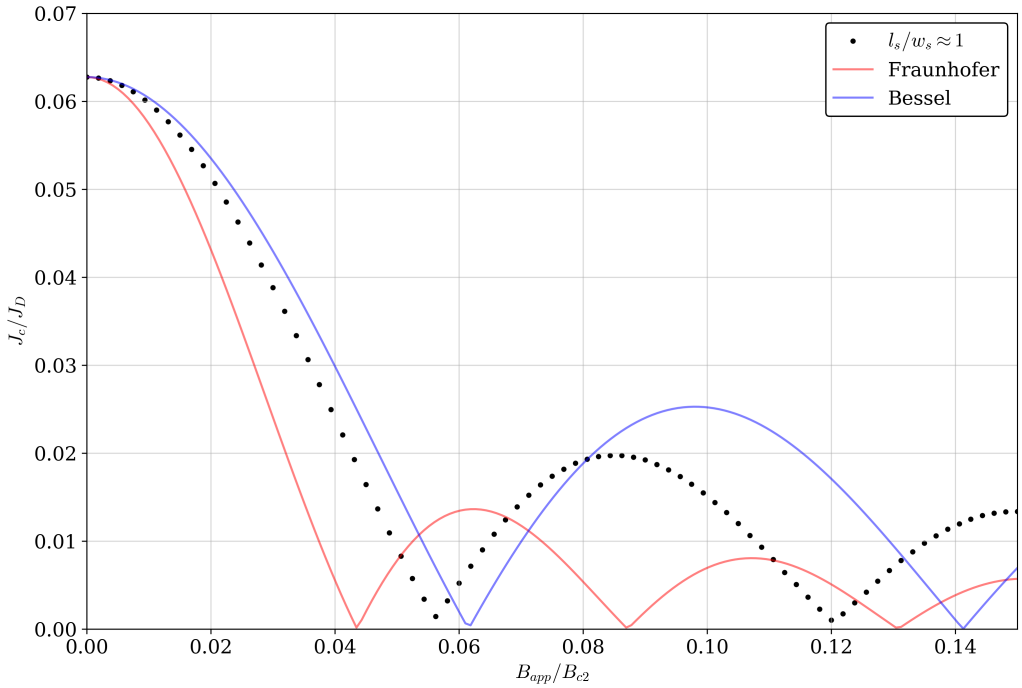


FIG. 4.i: The critical current density for a square junction of $w_s = 12\xi_s$, $l_s = 12\xi_s$ and thickness $d_n = 0.5\xi_s$ with $\alpha_n = -20$. The solutions for the short, Eq. (4.1.6) and long, Eq. (4.1.7) junction limits have been plotted with the data. As can be expected the junction with the square aspect ration falls between the two limits

The supercurrent in the y direction mostly curve away from the junction and as such vortices are more distantly spaced further apart at the edges than at the centre. This allows larger current densities to be carried in the edge regions and the critical current can be approximated to be [22],

$$J_c = J_{DJ}(0)\left|\mathfrak{J}_0\left(\frac{\pi\phi'}{\phi_0}\right)\right|, \qquad \text{where } \phi' = 14\zeta(3)B_{app}w_s^2/\pi^3 \tag{4.1.7}$$

here $\mathfrak{J}_0$ is the Bessel function of the first kind of order 0, $\zeta(3) = 1.202$ is the Riemann zeta function. We note that the zeroes, as given by the Bessel function, are not equally spaced unlike the sinc function. The equation is clearly closely related to diffraction equation for circular apertures given by the Airy function being $\mathfrak{J}_1(x)/x$. The data for an arbitrary weakly-coupled square junction can be seen in Fig. 4.i.

To gain an understanding of the change in the magnetic field dependence on the critical current as we add junctions in parallel to the first. We shall investigate the current around a large superconducting square loop with side length L and junction separation $D \gg \xi_s$ containing two weakly coupled junctions in parallel. Here the phase difference on either side of junction A and B is given as;

$$\Delta\theta_A - \Delta\theta_B = \frac{2\pi\phi}{\phi_0} \tag{4.1.8}$$

where $\phi = B_{\mathrm{app}}DL$ is the flux through the central area of the loop, with the area of the junctions assumed to be negligible, similar to the width of two slits compared to their separation

in the idealised double slit set up. The current density leaving the loop is thus a sum of the individual currents through the two junctions $J = J_A + J_B$, with each junction satisfying its own Josephson equation, Eq. (4.1.2), to give;

$$J = J_{DJ,A}\sin(\Delta\theta_A) + J_{DJ,B}\sin(\Delta\theta_B) \tag{4.1.9}$$

$$= J_{DJ}\sin(\Delta\theta_A) + J_{DJ}\sin\left[\Delta\theta_A - \frac{2\pi\phi}{\phi_0}\right] \tag{4.1.10}$$

where we have assumed the junctions share the same depairing current, $J_{DJ,A} = J_{DJ,B}$. The phase difference in the junctions will adjust to maximize the current through the loop and give by choosing the phase to be $\Delta\theta_A = \pi/2 + (\pi\phi)/\phi_0$. Thus the critical current for this loop is given by [24],

$$J_c = 2J_{DJ}\left|\cos\left(\frac{\pi\phi}{\phi_0}\right)\right| \tag{4.1.11}$$

This is the Josephson loop interference equation, the optical analogue being Young's double slit equation, where. In fact this is the basis of dc-SQUID magnetometer, which uses the destructive interference of the superelectron wavefunctions through the ring to measure the applied flux to an extremely small fraction of ϕ_0. As such, we shall use ideas from optical physics to ground our idea of what shall happen to the critical current of junction arrays and see which conditions in which this analogue is valid.

4.2 Altering Material Properties

In this first section we will now demonstrate the accuracy of the program by presenting data for a square electrode where we have altered the condensation parameter of the normal barrier. We will demonstrate that our data agrees with analytical solutions presented by Clem for narrow junctions in low fields, Eq. (4.1.4). For this work, the magnetic field has been increased up to a maximum value of $B_{\text{app}} \approx 0.15B_{c2}$. This approximately the maximum magnetic field possible before fluxons enter the electrode, causing an additional phase shift across the junction and altering the magnetic field dependence of depairing current $J_{DJ}(B)$. Going beyond this field, there is a decrease in the depairing current density that is not captured in any low field analytical solutions.

Within this framework, it is clear that the agreement between the analytical solution and the TDGL computational data seen in Fig. 4.ii dramatically improve as the weak junction assumption becomes more valid in the system and we see the data mapping towards this. As noted, the solution requires parameter optimisation for d_n of the junction to accurately capture the flux through the barrier and surrounding electrode, this reaches a value of $d_{\text{eff}} \approx 2.17\xi_s$ for the most negative condensation parameter. In addition to this the zero field junction depairing current density $J_{DJ}(0)$ has been set by the first data point to provide the amplitude. The oscillation in the critical current is clearly captured by the data, with a periodicity of the minima larger than $n\phi_0 = 2n\pi,\ n \in \mathbb{N}$, due the periodicity of the GI phase, Eq. (4.1.3). This is understood to be

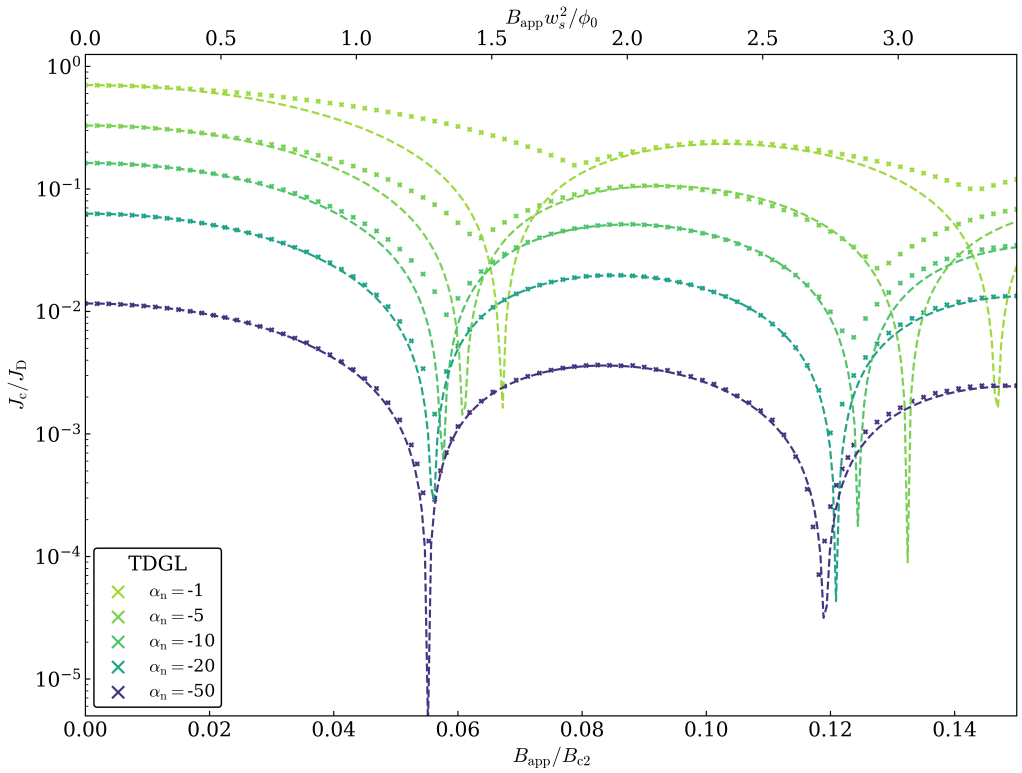


FIG. 4.ii: Critical current density for a square Josephson junction within a transverse magnetic field with electrode length of $l_s = 12.01\xi_s$ and width $w_s = 12.0\xi_s$ with $\kappa = 40$; the barrier is of thickness $d_n = 0.49\xi_s$ and has an effective mass $m_e = 1$. The α_n was varied between plots from $\alpha_n = -1$ up to $\alpha_n = -50$. The top x axis plots the flux through the system in units of ϕ_0. The analytical solution of Eq. (4.1.4) has been plotted by the dotted lines in the figure

a result of fluxons moving into and out of the barrier and altering the phase shift between the electrodes and thus the critical current.

4.3 Junction Arrays

In this section we shall present data of junction arrays, first we shall demonstrate that our code is accurate for generating array data by confirming our data with that of Din's. Then we will present data for the critical current of new arrays and compare this to the individual junctions that have formed the array counterpart. We will also present approximation and empirical techniques to predict the critical current of these system and qualitatively compare their fit. A replication of Din's junction array [25] is displayed by section 4.3.

The critical current dependence on the magnetic field of this system is provided in the following section 4.3, up to a magnetic field strength of $0.2B_{c2}$. It can be seen that there is good agreement between our data for the initial zero field junction depairing current density, as well as the periodicity and value of the current density for half the plot range. This is until there is a loss in fidelity the data at higher fields and the oscillation and amplitude reduces. I believe that

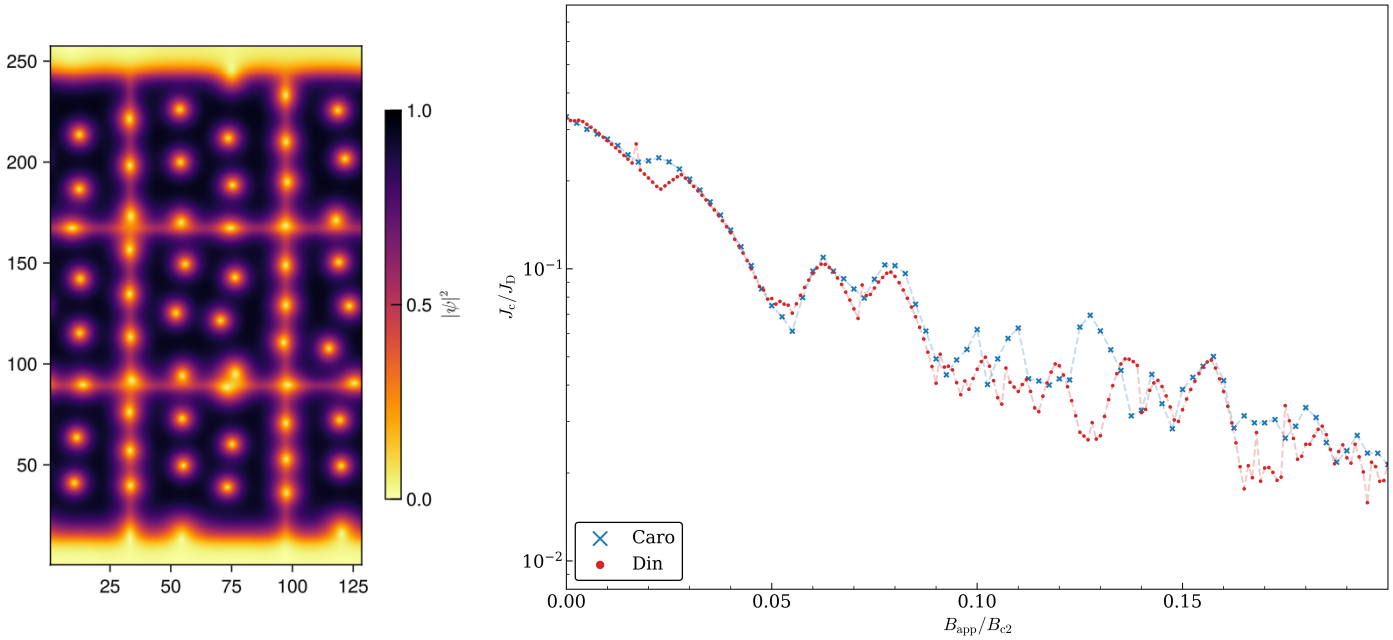


FIG. 4.iii: (Left) A $(2, 3)$ junction array, where the single junction electrode has width $w_s = 16\xi_s$ and length $l_s = 16\xi_s$, with junction thickness $d_{n,x} = 0.5\xi_s$. The coating of the junction unit cell is now equal to the junction thickness of $d_{n,y} = 0.5\xi_s$, to represent the polycrystalline grain boundaries and there is a total outer coating of width $w_c = 6\xi_s$. The total width of the system is $w_t = 55\xi_s$ and length $l_t = 33\xi_s$ and the material parameters are $\alpha_n = -1$ and $\kappa = 8$. (Right) The critical current density as a function of field for the junction array.

there is a combination of reasons this. One is that I have used a larger grid spacing than Din, with $h \approx 0.2\xi_s$ compared to $0.1\xi_s$, which due to the small junction thickness $d_n = 0.5\xi_s$ causes a decrease in the accuracy of the data at higher fields where the system dynamics becomes more complicated. But namely I believe that the disagreement is due to the low κ value of the superconducting material in simulation. Here $\kappa = 8$ and so $\lambda_s = 8\xi_s$, whereas the width of the system is $w_s = 16\xi_s$. This means we are working more closely to the wide junction regime of $w_s \gg \lambda_s,\ \xi_s$. In this regime as demonstrated by Blair [22], the critical current take multivalued solutions in $J_c(B)$, the value found partly depending on the direction of approach of the applied field. As such, due to possible differences in our program methodology the final critical current may take different values.

As the data is in suitable good agreement with Din within small magnetic fields we shall continue onto new data for Josephson junction arrays and demonstrate how they reproduce effects seen in multiple slit optical diffraction and methods to model the critical current.

4.3.1 Junctions in Series and Parallel

The data in this section is for junctions in series and parallel and we will demonstrate that in many cases they behave as expected. We shall also look into a qualitative understanding and

empirical equations to predict the critical current of the array systems and discuss the accuracy of these methods.

First we shall add a second junction, with the same dimensions, in series with the first. There is limited information in the literature that describes the change in the critical current in this case. However, from our understanding of the optical properties of junctions seen in section 4.1.2, we expect that there should be no change on the critical current of the system. As, for light that propagates through a series of individual slits, each successive slit in an idealised scenario behaves as a point source. Hence only the final slit in the series determines the interference pattern.

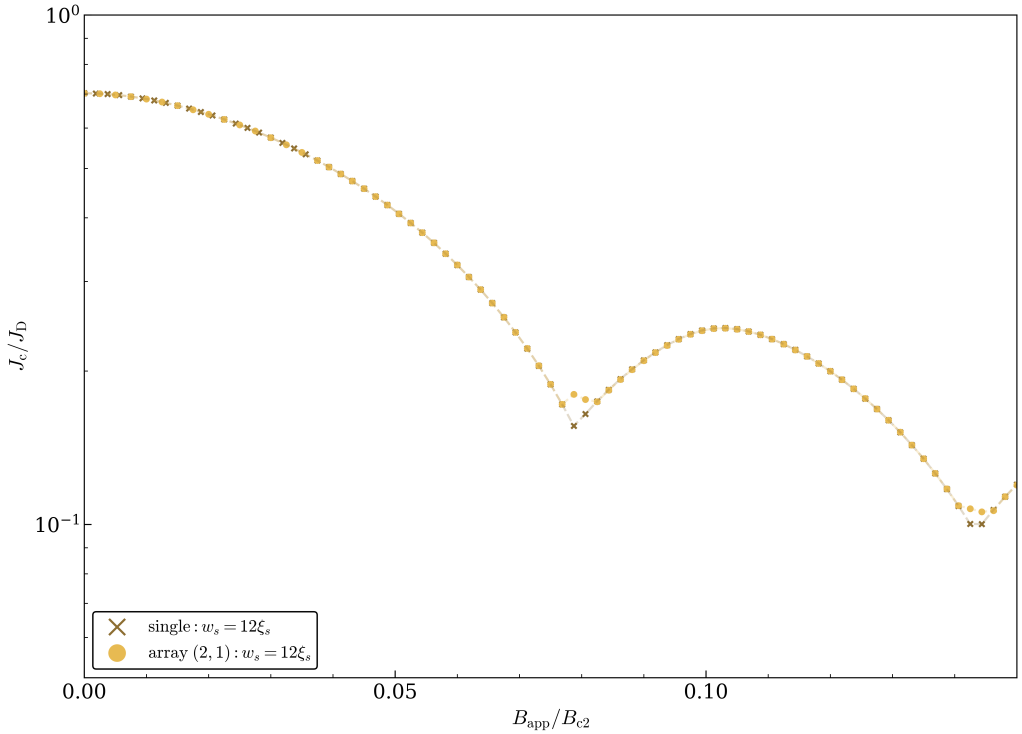


FIG. 4.iv: The critical current density as a function of field for a $(2, 1)$ junction series. The single junction has $w_s = 12\xi_s$ and $l_s = 12\xi_s$ with $d_n = 0.5\xi_s$ with no coating. The material parameters are $\alpha_n = -1$ and $\kappa = 40$

We can see some interesting data presented in Fig. 4.iv, we see that the critical current of the system closely follows the critical current of the single junction for the majority of the magnetic field range. Suggesting that the phase difference between each electrode, as given by Eq. (4.1.3), is not different from the single junction case over this range and supporting our intuition of the system gained from the optical analogue, a simplistic view as it may be. But it does indeed display a notable difference with the optical case. For the junction in series, there are small peaks or flattened minima, where we find minima for the single junction. It is difficult to provide an explanation for this occurrence. However, the gauge invariant phase difference across the junction must be very similar to the single junction case.

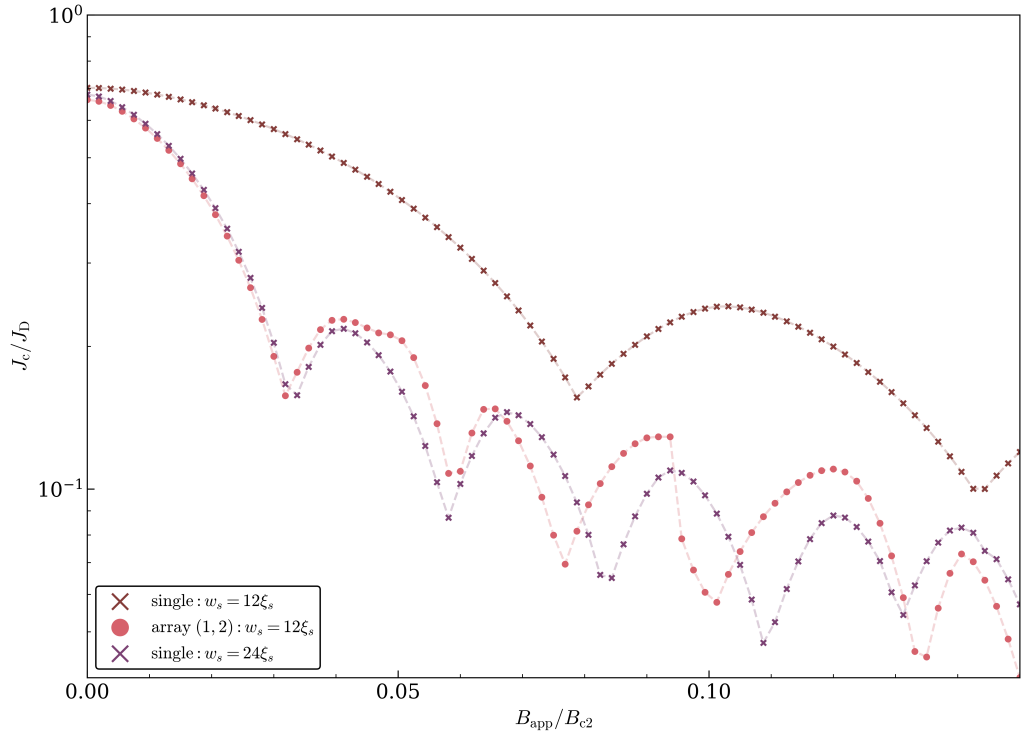


FIG. 4.v: The critical current density as a function of field for a $(1, 2)$ junction in parallel. The single junction has $w_s = 12\xi_s$ and $l_s = 12\xi_s$ with $d_n = 0.5\xi_s$ with an outer coating of $w_c = 0.25\xi_s$. The material parameters are $a_n = -1$ and $\kappa = 40$.

Adding a second identical junction in the y direction creates a parallel junction system and we may examine our equations from section 4.1.1 to understand the effect. We see that as our system is now twice as large as the individual case, the flux through the system must double as well. In the narrow junction limit, where we have high κ, the assumption is that the magnetic field penetrates the entirety of the junction equally, with screening currents throughout. If the barriers between the parallel junctions make a negligible difference to the system due to strong coupling between electrodes, with a strong proximity effect maintaining a non-zero order parameter through the barrier [17]. Then we may expect the periodicity to change as predicted by the single junction diffraction equations, Eq. (4.1.6) and Eq. (4.1.7), and thus double in frequency.

However we do not see this in Fig. 4.v, the frequency in the minima appears to triple for both the parallel and wide junction compared to the original case. We can reconcile this with the fact that the original junction has a square aspect ratio, so for the wider parallel junction it more accurately agrees with the short junction limit of Eq. (4.1.6). Thus our previous analysis is an over simplification and it is difficult to accurately discuss the periodicity change in this context. Comparing the data of the parallel junction with a junction with the same total electrode width of $24\xi_s$, we see that, indeed, the periodicity of the parallel junction system and of the wide junction are quite similar; though the parallel junction periodicity is slightly shorter and interestingly does not appear to be constant. However it supports an idea that for strongly coupled parallel junction system, a glass array may be representative of this parallel system, where the

order parameter in each electrode affects the others.

4.3.2 Optical Analogues

Thus to apply our optical understanding of parallel junctions, we must investigate the system in the weakly coupled limit, with the aim to replicate finite width slit diffraction. To build an empirical equation for $J_c(B)$, we expect the resulting current to be a product of the single junction and parallel junction equations, which represent Eq. (4.1.4) and Eq. (4.1.11) respectively, where the first is the flux through the barrier and the second is the flux through the total system. The resulting equation, however, would not be able to describe the critical current of a single narrow junction, like we expect of a multi-slit equation in optics. This motivates us to take the direct diffraction grating equation and modify it for our use, we may write our resulting equation as,

$$J_c = \frac{J_{DJ}(0)}{n_y w_{\text{eff}}} \left| \int_{-w_{\text{eff}}/2}^{w_{\text{eff}}/2} dy \sin\left(\Delta\gamma(y)\right) \right| \left| \frac{\sin(n_y \pi\phi/\phi_0)}{\sin(\pi\phi/\phi_0)} \right| \tag{4.3.1}$$

where $\phi = n_y w_{\text{eff}} l_{\text{eff}}$, represents the total flux through the array, with w_{eff}, l_{eff} being the effective width and length of the junction and n_y the number of parallel junctions. The GI phase difference, $\Delta\gamma(y)$, as seen in Eq. (4.1.3), also uses these optimised parameters w_{eff}, l_{eff} and d_{eff}. An additional factor of $1/n_y$ is added to the equation to offset the amplitude scaling of the diffraction grating equation, where $|E| \propto N$ for an electric field from an N aperture grating is not seen in the case of a junction. The optimised parameters are required due to the nature of an empirical solution, but may be a result of the high κ limit not being well satisfied in a system which is twice as large as seen in Fig. 4.ii, so cannot assume a constant magnetic field in the system. As we have done for previous solutions, we use the first data point to provide the amplitude of oscillation of the current $J_{DJ}(0)$.

The equation Eq. (4.3.1) has been plotted against data for a $(1, 2)$ array with the usual single junction dimensions. Very good agreement can be seen between the data and critical current density function. The optimised parameters for the electrode width, length and junction thickness are seen in Table. II. More investigation into the empirical solution is needed to understand its agreement with additional parallel junctions and those with varying geometries. A discrepancy between the predicted empirical value and the amplitude of the critical current data can be seen at higher fields. At these fields, it is unlikely to be due to fluxons entering the junction and may be an effect of the coating left on the system due to issues in array generation. However, the agreement between solution and data does demonstrate that it captures some of the dynamics of the parallel junction system. The requirement of optimised parameters, possibly due to the inaccuracy of the narrow junction approximation, however indicate that the relationship between flux penetration and electrode phase difference is currently incorrectly described.

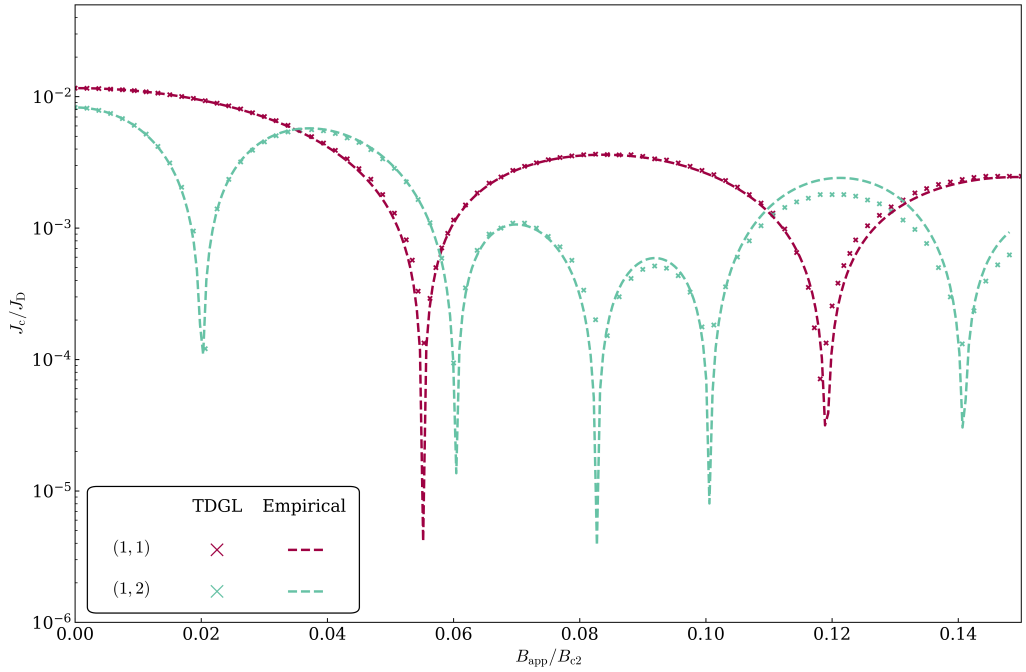


FIG. 4.vi: Data and empirical solution comparison for a weakly-coupled $(1, 2)$ junction array and single junction. The single junction has dimensions $w_s = 12\xi_s$, $l_s = 12\xi_s$ and $d_n = 0.5\xi_s$ with no coating; the material parameters are $a_n = -50$ and $\kappa = 40$. The array has a total size of $w_t = 25\xi_s$ and $l_t = 12.5$ and includes an outer coating of $w_c = d_n/2$. The empirical equation Eq. (4.3.1) uses $d_{\text{eff}} \approx 2.18\xi_s$ for the single junction and those for the array are shown in Tab. II

	Dimension		
	Width	Length	Thickness
Parameter	$(0.86 \pm 0.10)w_s$	$(0.63 \pm 0.07)l_s$	$(5.12 \pm 2.87)d_n \approx 3\xi_s$

TABLE II: Values of the optimised dimensions for the $(1, 2)$ junction array

5 Conclusions & Further Work

This thesis has presented an investigation into novel junction systems and provided an overview of the effect of series and parallel junction arrays on the critical current as a function of field with comparisons to the singular junction counterparts. We have made use of analytical frameworks developed by previous research within the Durham Superconductivity research group and those well known in the field of superconductivity. In addition to this, we presented analysis of certain superconducting junction systems through their optical analogues and made note on how the condensation parameter α_n of the systems effects this analogy. This has provided us with one perspective that strongly coupled systems may be viewed as larger single junctions with electrode width equal to total electrode width in the parallel system. The other, a quantitative argument whereby weakly coupled parallel arrays can be seen to replicate optical

systems.

Initially we demonstrated that our code, using the Julia package 'MulTDGL', can reliably simulate superconductors by replicating work done by Din and Blair. Plotting the average electric field against current of a superconductor as seen in Fig. 3.iii we gained a better understanding of the transitive states displayed by a superconductor transitioning from the superconducting to the normal state. This allowed us to identify when a superconductor enters the flux flow regime thereby losing perfect conductivity and providing our criterion for the critical current density J_c. Following this we compared critical current data for a square junction to analytical solutions developed by Clem for narrow, high κ superconductors in low fields (Fig. 4.ii) and then for an arbitrary array generated by Din (section 4.3), seeing good agreement in each.

When we investigated a narrow weakly coupled array, we saw that, unlike systems with small α_n, where the proximity effect maintains the order parameter within the normal barrier between junctions, the weakly coupled system presents a strong analogue to multi-slit optics. This, we understood, was due to the increased suppression of the order parameter within the barriers, allowing the wavefunctions of the parallel junctions to behave separately. Thus providing clear wavefunction interference, as predicted by double slit optics. From taking the product between the known solution of diffraction gratings and those derived for weakly couple narrow junctions, we produced a good empirical solution for the data.

With more time, it would be good to make better use of the highly versatile MulTDGL package and investigate a wider range of array geometries and material properties, including altering the effective mass and a range of magnetic fields more relevant for industry use. In addition, as the investigation only included junctions in series and parallel, it would be beneficial to extend this to square or rectangular arrays. With this we may hope to provide more detailed and rigorously defined analytical solutions for the critical current density functional form of these junctions. However, due to the time requirements in producing individual plots, especially in highly negative α_n systems, where the relaxation time dramatically increases and the critical current varies significantly, there was a limited amount of suitable data collected. In addition to this, there can be an improvement in the generation of accurate geometric systems, with issues of 'off-by-one' errors in interface locations and system geometry within Julia arrays that limit the accuracy of the data collected, including the error noted in array generation that produced an minimum external coating.

In this paper we have only considered a single, perpendicular angle of magnetic field intersection and superconducting systems that do not display anisotropic α_s values. But, as shown by Tinkham [26] for an ISI system and Hylton and Beasely [27] for magnetic penetration into grain boundaries, this orientation angle indeed plays an important effect on the critical field of the system. While work by Hilgenkamp [28] has shown that the relative orientation of these crystals affects the current density that can propagate between grains, which can be described by a change in effective α_s and α_n values of neighbouring grains and grain boundaries. As such, many more properties need to be considered in junction arrays until they may be used to model real polycrystalline superconductors even on the very small scale.

Acknowledgments

I would first like to thank my project supervisor D. P. Hampshire for his insightful guidance and advice throughout my project. In addition I'd like to thank the PhD students in the Durham superconductivity research group, including Y. A. Nasir who provided support during my two terms of research. Finally I'd like to acknowledge the use of Durham University's NCC cluster, which made this work possible, that was installed and is maintained by the Department of Computer Science through funding by Durham University's strategic investment funds.

References

[1] H Kamerlingh Onnes. Further experiments with liquid helium. c. on the change of electric resistance of pure metals at very low temperatures etc. iv. the resistance of pure mercury at helium temperatures. In KNAW, Proceedings, volume 13, pages 1910–1911, 1911.

[2] Walther Meissner and Robert Ochsenfeld. Ein neuer effekt bei eintritt der supraleitfähigkeit. Naturwissenschaften, 21(44):787–788, 1933.

[3] Jury N Rjabinin and LW Shubnikow. Magnetic properties and critical currents of supra-conducting alloys. Nature, 135(3415):581–582, 1935.

[4] Vitaly L Ginzburg and Lev D Landau. On the theory of superconductivity. Zh. Eksp. Teor. Fiz., 20:1064–1082, 1950.

[5] Brian David Josephson. Possible new effects in superconductive tunnelling. Physics letters, 1(7):251–253, 1962.

[6] Sidney Shapiro. Josephson currents in superconducting tunneling: The effect of microwaves and other observations. Physical Review Letters, 11(2):80, 1963.

[7] BRIAN D Josephson. The discovery of tunnelling supercurrents. Reviews of Modern Physics, 46(2):251, 1974.

[8] Elliot Snider, Nathan Dasenbrock-Gammon, Raymond McBride, Mathew Debessai, Hiranya Vindana, Kevin Vencatasamy, Keith V Lawler, Ashkan Salamat, and Ranga P Dias. Retracted article: Room-temperature superconductivity in a carbonaceous sulfur hydride. Nature, 586(7829):373–377, 2020.

[9] Michael Tinkham. Ginzburg-landua thoery. In Introduction to Superconductivity, chapter 4, pages 110–143. Dover Publiations, 2 edition, 2004.

[10] Albert Schmid. A time dependent ginzburg-landau equation and its application to the problem of resistivity in the mixed state. Physik der kondensierten Materie, 5(4):302–317, 1966.

[11] Lev Petrovich GOR'KOV and GM Eliashberg. Generalization of the ginzburg-landau equations for non-stationary problems in the case of alloys with paramagnetic impurities. In 30 Years Of The Landau Institute—Selected Papers, pages 16–22. World Scientific, 1996.

[12] Chia-Ren Hu and Richard S. Thompson. Dynamic structure of vortices in superconductors. ii. $h \ll H_{c2}$. Phys. Rev. B, 6:110–120, Jul 1972.

[13] PGf de Gennes. Boundary effects in superconductors. Reviews of Modern Physics, 36(1):225, 1964.

[14] William D Gropp, Hans G Kaper, Gary K Leaf, David M Levine, Mario Palumbo, and Valerii M Vinokur. Numerical simulation of vortex dynamics in type-ii superconductors. Journal of Computational Physics, 123(2):254–266, 1996.

[15] T Winiecki and CS Adams. A fast semi-implicit finite-difference method for the tdgl equations. Journal of Computational Physics, 179(1):127–139, 2002.

[16] IAN BLAIR, ALEXANDER. Simulations of Critical Currents in Polycrystalline Superconductors Using Time-Dependent Ginzburg-Landau Theory. PhD thesis, Durham University, 2021.

[17] BRADLEY PETER DIN. Computational and Analytic Time-Dependent Ginzburg-Landau Theory for High-Resistivity High-Field Superconducting Josephson Junctions. PhD thesis, Durham University, 2024.

[18] CWW Haddon and DP Hampshire. Fast multigrid simulations of pinning in rebco with highly resistive nanorods. IEEE Transactions on Applied Superconductivity, 33(5):1–5, 2023.

[19] William F Ames. Numerical methods for partial differential equations. Academic press, 2014.

[20] IA Sadovskyy, AE Koshelev, Carolyn L Phillips, Dmitry A Karpeyev, and Andreas Glatz. Stable large-scale solver for ginzburg–landau equations for superconductors. Journal of Computational Physics, 294:639–654, 2015.

[21] John R Clem. Josephson junctions in thin and narrow rectangular superconducting strips. Physical Review B—Condensed Matter and Materials Physics, 81(14):144515, 2010.

[22] IAN BLAIR, ALEXANDER. Simulations of Critical Currents in Polycrystalline Superconductors Using Time-Dependent Ginzburg-Landau Theory. PhD thesis, Durham University, 2021. See Chapter 4.2: Weakly Coupled SNS Junctions in Low Magnetic Fields.

[23] B Bonin. Materials for superconducting cavities. 1996.

[24] Charles P Poole, Horacio A Farach, Richard J Creswick, and Ruslan Prozorov. Energy gap and tunneling. In Superconductivity, chapter 15, pages 433–486. Elsevier, 2 edition, 2007.

[25] BRADLEY PETER DIN. Computational and Analytic Time-Dependent Ginzburg-Landau Theory for High-Resistivity High-Field Superconducting Josephson Junctions. PhD thesis, Durham University, 2024. See Chapter 5.6: Junction Arrays.

[26] Mer Tinkham. Effect of fluxoid quantization on transitions of superconducting films. Physical Review, 129(6):2413, 1963.

[27] TL Hylton and MR Beasley. Effect of grain boundaries on magnetic field penetration in polycrystalline superconductors. Physical Review B, 39(13):9042, 1989.

[28] Hans Hilgenkamp and Jochen Mannhart. Grain boundaries in high-t c superconductors. Reviews of Modern Physics, 74(2):485, 2002.

Summary for a General Audience

Superconductors are materials that can carry electricity without any energy loss, unlike the wires in homes and cities that waste energy as heat due to their resistance. This remarkable ability is only possible when the material is extremely cold, sometimes comparable to the temperature of outer space. This special property of perfect conductivity allows the material to carry vast currents and thus generate powerful magnetic fields. These properties underpin technologies such as MRI machines, particle accelerators, and future fusion reactors, where the large fields generated and efficient current flow are essential.

This project looks at a special type of superconductor structure known as a Josephson junction, where thin barriers interrupt the flow of superconducting current. These junctions can provide understanding into how real-world superconductors behave, due to the similarities between these junctions and the tiny crystals that make up superconductors. Through advanced computer simulations, the project explores how much current these junctions can carry before losing their superconducting state - their critical current - and how this value depends on the presence of magnetic fields which they are in.

A better understanding of this property and how it changes under different fields and junction geometries can help us develop better superconductors with larger critical currents. With applications from medical imaging to potential future energy sources, this research provides insight into how we can improve the performance of superconductors by understanding the role of their microscopic structure—bringing us closer to technologies that are faster, more efficient, and entirely lossless.

Statement of gAI Use

Both ChatGPT 4.0 and GitHub copilot using ChatGPT 1o have been utilised in making this thesis. With ChatGPT 4.0 aiding in research and understanding of aspects of the theory and computational methods used in this project and GitHub copilot as an aid for writing the program code in Julia and for Python plots.

Appendix

A NCC GPU Computing & Example Code

Multigrid methods benefits from highly parallelisable computation, as grid levels that can be solved in parallel to find residual solutions on each. In addition to this Gauss-Seidel iteration only depends on neighbouring grid points, thus on a structured grid, both equation updates and the final residual interpolation between grids, may be performed independently on non-overlapping regions. This all increases computing speed when the code is run on GPUs.

However it still requires very powerful GPUs to run the program in efficient time, as such I have made use of the large GPU array provided by the Computer Science department named the NVIDIA CUDA Centre (NCC). This provides me with access to a maximum of 4 high powered GPUs at one time and 250 Gb of storage space in my local directory.

Create and then update the simulation:

```
# initial state
fluxoncount = ((0, 0), (0, 0)) # used for quasiperiodic boundary conditions
ψdata = adapt(backend, exp.(2π * im .* rand(Float64, elemcount(m, Val(0)))))
ψ = RectWavefunctionData(m, fluxoncount, ψdata)
a = RectPrimalForm1Data(m, KernelAbstractions.zeros(backend, Float64, elemcount(
    m, Val(1))))
ϕ = RectPrimalForm0Data(m, KernelAbstractions.zeros(backend, Float64, elemcount(
    m, Val(0))))
u = RectPrimalForm1Data(m, KernelAbstractions.ones(backend, ComplexF64,
    elemcount(m, Val(1))))
st = State(ψ, a, ϕ, u)

# create simulation
s = MulTDGL.ImplicitLondonMultigridSolver(m, p, mat, st, tol, levelcount)

@time step!(s, bcs)                              # evolve system by 1 timestep
```

Calculate the average modified link variables of Winiecki (the phases of Gropp's unimodular link variables) used in E-field calculations:

```
function a1_avg(s::ImplicitLondonMultigridSolver)
    e_buffer = MulTDGL.similar(state(s).a)
    data(e_buffer) .= data(state(s).a)
    set_form!(e_buffer, MulTDGL.mesh(s)) do e, e_buf, m
        e_buf[e] * measure(m, dual(e))
    end
    sum(asarray(e_buffer, 1)) / measure(MulTDGL.mesh(s))
end
```

Create an α Julia array for the system geometry:

```
for row in 0:(array_ny - 1)
    for col in 0:(array_nx -1)
```

```
        if d_ny != 0 || w_cy != 0
            # COATING
            asarray(α)[(1+col*l):((col+1)*l + (col==(array_nx-1) ? w_cx : 0)), (
                1+(row*w)+w_c1):(d_ny1+(row*w)+w_c1)] .= α_c              #
                bottom coating
            asarray(α)[(1+(col*l)):(l_s1+(col*l)+1), ((row*w)+w_c1+d_ny1+1)] .=
                (α_c+1)/2                                                 #
                bottom-left interface
            asarray(α)[((col+1)*l-l_s2+1):((col+1)*l + (col==(array_nx-1) ? w_cx
                 : 0)), ((row*w)+w_c1+d_ny1+1)] .= (α_c+1)/2              #
                bottom-right interface
            asarray(α)[(1+(col*l)):(l_s1+(col*l)+1), ((row+1)*w+w_c1-d_ny2+1)] .
                = (α_c+1)/2                                               # top-
                left interface
            asarray(α)[((col+1)*l-l_s2+1):((col+1)*l + (col==(array_nx-1) ? w_cx
                 : 0)), ((row+1)*w+w_c1-d_ny2+1)] .= (α_c+1)/2            # top-
                right interface
            asarray(α)[(1+col*l):((col+1)*l + (col==(array_nx-1) ? w_cx : 0)), (
                (row+1)*w+w_c1-d_ny2+2):((row+1)*w+w_c1+1)] .= α_c        # top
                coating
        end
        if d_nx != 0
            # JUNCTION
            asarray(α)[(l_s1+(col*l)+1), ((row*w)+w_c1+d_ny1+1):(array_ny==1 ?
                end-w_c2 : (row+1)*w+w_c1-d_ny2+1)] .= (α_d+1)/2        # left
                interface
            asarray(α)[(l_s1+(col*l)+2):((col+1)*l-l_s2), ((row*w)+w_c1+d_ny1+1)
                :((row+1)*w+w_c1-d_ny2+1)] .= α_d                        #
                junction
            asarray(α)[((col+1)*l-l_s2+1), ((row*w)+w_c1+d_ny1+1):(array_ny==1 ?
                 end-w_c2 : (row+1)*w+w_c1-d_ny2+1)] .= (α_d+1)/2      # right
                interface
        end
    end
end
```

B Trialled Ramping Methods

Current ramping methods, rates and hold times were modified to determine the most effective and fastest method of reaching the critical current. The program would not experience a noticeable increase in calculation time for larger current steps and systems relax at linear, but quite rapid, rate. So the code would not take significantly longer to ramp and relax for larger current steps and reach J_c in less time. However, of course, this would come at the expense of resolution and accuracy of the critical currant. The hold time was another parameter that had a significant impact on the time to determine the critical current, it was important to make it long enough to allow for transient effect to occur and to allow for two full oscillations to occur above E_c. But of course after the critical current oscillations will occur indefinitely, so any time spent here would be wasted.

Both individual linear and exponential current ramps were trialled. Linear ramping methods, provided a steady and reliable current ramp, however the smallest critical currents that can be determined is limited by the ramp step, and determined the time taken to find the largest critical current densities in the field range. So an exponential ramp rate was trialled, in which the current

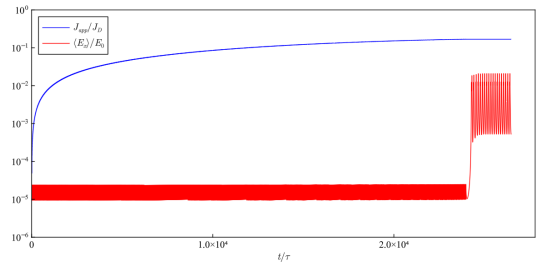


FIG. B.i: Linear ramping

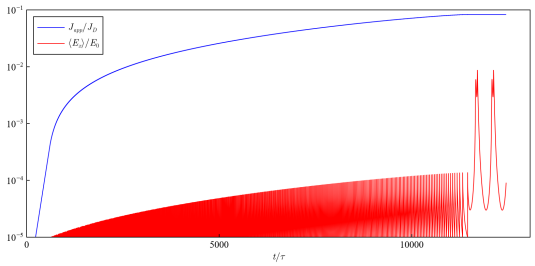


FIG. B.ii: Exponential ramping

was increase by 1% at each step. Though this increased program speed, it reduced the accuracy of the final current determined, with the largest ramp rates occurring just before the onset of the resistive state, so lacked precision in determining J_c. However, it provided the benefit of sweeping through a large range of currents with relative speed. Examples of the two methods used individually can be seen in Fig. B.i and Fig. B.ii

C Additional Array & Junction Data

Additional data for square arrays and 'short' junctions are shown below. Good periodicity can be seen in the highly negative α_n, $(2, 2)$ array of **????** as well as the 'short' junction in Fig. C.iii, agreeing well with Eq. (4.1.2) at larger magnetic fields.

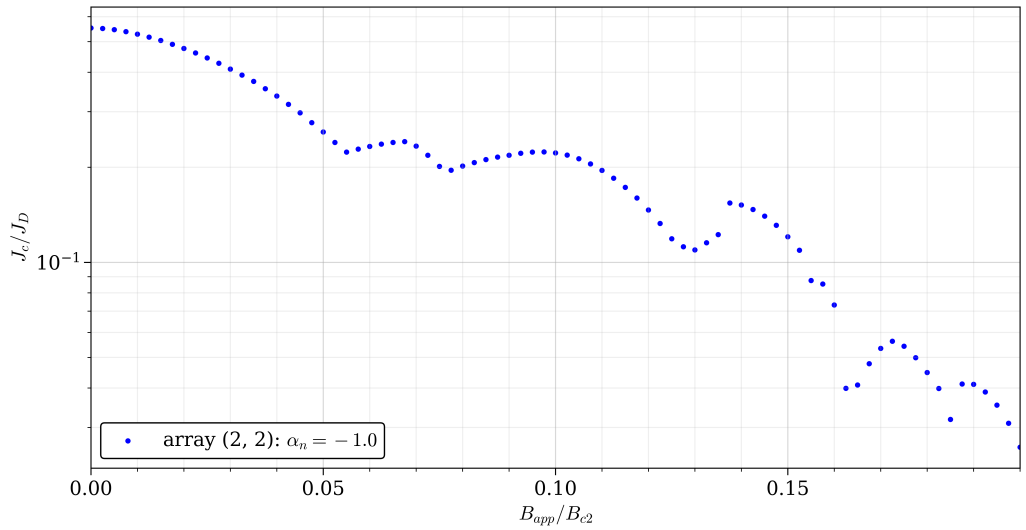


FIG. C.i: Critical current for a (2, 2) array with $w_s = 7.5\xi_s$, $l_s = 7.5\xi_s$ and $d_n = 0.5\xi_s$, with a normal material material parameters of $\alpha_n = -1, m = 1$

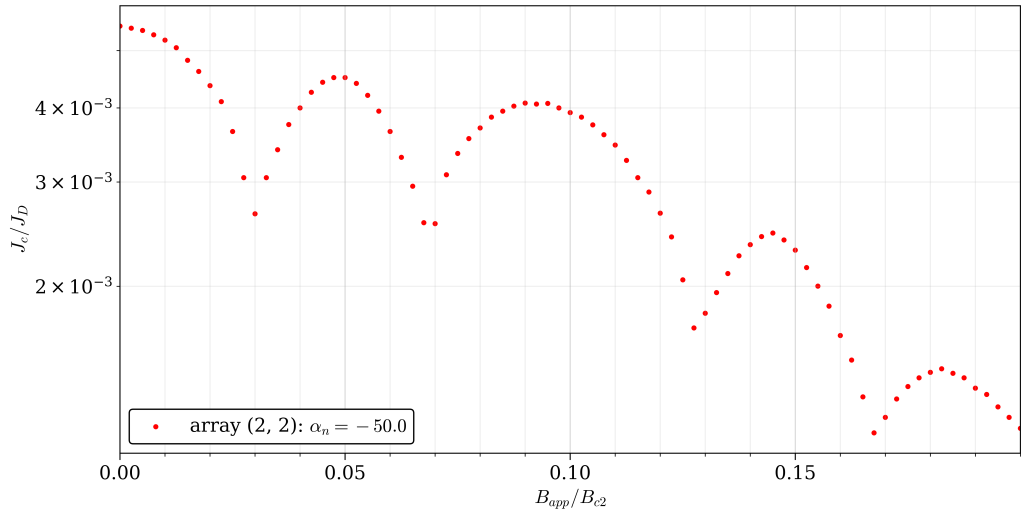


FIG. C.ii: Critical current for a (2, 2) array with $w_s = 7.5\xi_s$, $l_s = 7.5\xi_s$ and $d_n = 0.5\xi_s$, with a normal material material parameters of $\alpha_n = -50, m = 1$

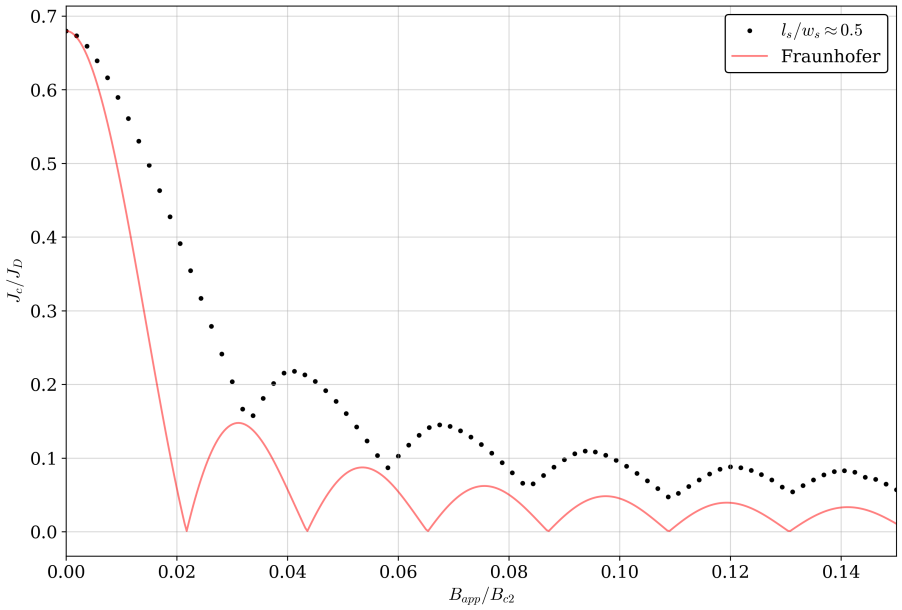


FIG. C.iii: Short junction Fraunhofer solution plotted with data from a junction with dimensions: $w_s = 24\xi_s, l_s = 12\xi_s$ and $d_n = 0.5\xi_s$